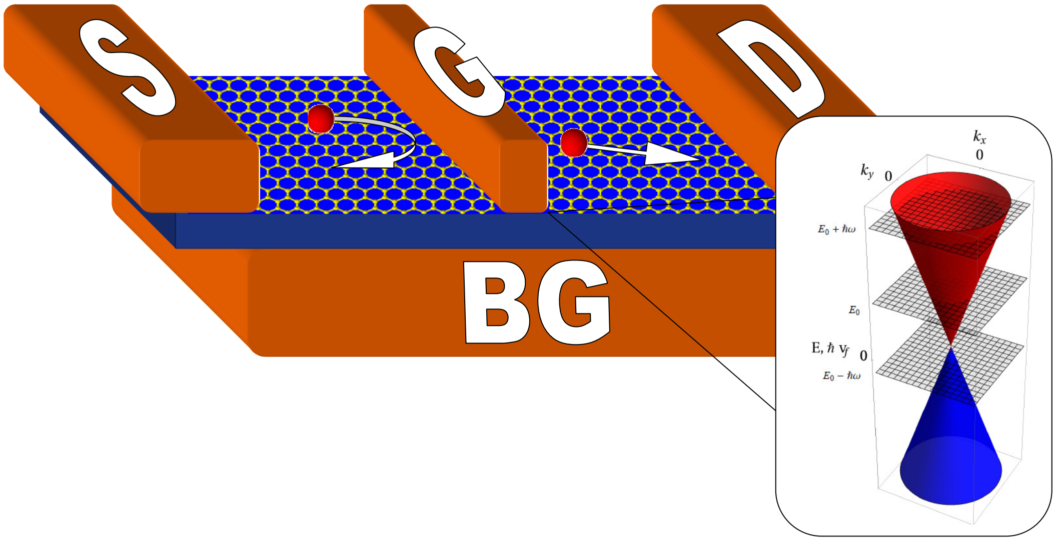

BALLISTIC ELECTRONIC TRANSPORT THROUGH AN OSCILLATING BARRIER IN GRAPHENE

Yevgeniy Korniyenko

Department of Microtechnology and Nanoscience
CHALMERS UNIVERSITY OF TECHNOLOGY
Göteborg, Sweden 2011

Thesis for the Degree of Master of Science

Ballistic electronic transport through an oscillating barrier in graphene

YEVGENIY KORNIYENKO

Department of Microtechnology and Nanoscience
CHALMERS UNIVERSITY OF TECHNOLOGY
Göteborg, Sweden 2011

Ballistic electronic transport through an oscillating barrier in graphene

YEVGENIY KORNIYENKO

Department of Microtechnology and Nanoscience
Chalmers University of Technology
SE-412 96 Göteborg, Sweden
Telephone +46(0)31-772 1000

Cover: the picture on the title page shows a graphene-based transistor. The inset shows a low-energy dispersion relation of graphene with energy sidebands due to scattering from oscillating potential.

Chalmers Reproservice
Göteborg, Sweden 2011

Ballistic electronic transport through an oscillating barrier in graphene
YEVGENIY KORNIYENKO
Department of Microtechnology and Nanoscience
Chalmers University of Technology

Abstract

Graphene is a novel material with prospective use in new electronic devices. Its various properties and potential applications are still under large-scale studies. One of the active research areas is oriented towards development of a graphene-based high-frequency transistor with technical characteristics that might top the current semiconductor-based devices. This thesis concentrates on a scattering problem in one such graphene device driven with static and time-periodic external voltages.

The electrical conductance through a four-terminal graphene device is examined from a quantum-mechanical point of view. A high static barrier scattering problem is solved and demonstrated to be in agreement with previous results. Differences between graphene-based and Schrödinger-type systems are highlighted.

Corrections to the static conductance are obtained for AC perturbation to static potential. Formation of energy sidebands and their relation to driving parameters is examined in details. Generation of bound states is investigated in the framework of the first-order perturbation theory. Finally, the adiabatic limit is presented and the range of parameters where this limit is relevant is discussed.

Noise calculation is presented for the case of static driving. Results for zero-frequency noise and Fano factor are obtained and compared with graphene-based systems with different layouts.

Keywords: graphene, oscillating barrier, conductance, zero-frequency noise

Acknowledgements

Using the moment, I would like to express my deepest gratitude to people who contributed to this work, in one way or another.

This sheet of paper cannot contain the amount of thankfulness which goes to my supervisor, Tomas Löfwander. I greatly appreciate the time he has devoted to passing a part of his knowledge in physics into my head, even over my persistent stonewalling. I acknowledge an amount of fruitful discussions on various parts of the research and physics in general. Deepest thanks for being always supportive and ready to answer my endless questions, and providing valuable help and guidance even regarding non-academic matters of mine.

I am grateful to members of AQP and QDP groups for running a little warm community of ours. Tuesday meetings proved to be always scientifically stimulating and often entertaining. I would like to thank Vitaly Shumeiko for important discussions regarding my research, and all senior members of our group for giving me food for thought. Many thanks go to my lab fellows for all the laughs and cheers shared during coffee and non-coffee breaks. I would like to thank my opponents, Ian Kellett and Abhilash Ram, for taking on the task of showing me different points of view on the topic.

I acknowledge Swedish Institute for the support given through the Visby Program scholarship. If not for this funding, I would not be able to enjoy life and studies in such a wonderful country as Sweden is.

Finally, my warmest thanks go to my family. And by family I mean not only my parents and relatives, but also friends whose support and love indeed made it a home-like experience wherever I was. I would like to thank the most important people in my life: my mom, dad, and grandma,- for being always there for me, for endless care and love, for their worries with or without a reason; I sincerely tried to give them less of the latter. Special thanks go to "Kiruna & Co." guys for wonderful time spent together.

Contents

Nomenclature

$2DEG$	Two-dimensional electron gas
FET	Field-effect transistor
$1D$	One dimensional
$2D$	Two-dimensional
DC	Direct current
AC	Alternating current
SE	Schrödinger equation
FF	Fano factor
Tr	Trace of a matrix
H	Hamiltonian
v_F	Fermi velocity in graphene
$\sigma_{x,y}$	Pauli matrices
h	Planck constant
$\hbar$	Reduced Planck constant
Ψ	Wavefunction of a charge carrier
E	Energy of a charge carrier
K, K'	Dirac points
$\phi_{A,B}$	Atomic wavefunctions
$\vec{k}$	Wavevector of a particle
$\vec{j}$	Probability current density
V_0	Static barrier height
D	Barrier width
V	AC perturbation to barrier height
t	Time
t_n	Tunneling amplitude of n^{th} sideband
r_n	Reflection amplitude of n^{th} sideband
$\hat{s}$	Scattering matrix
ϕ_n	Angle of incidence at n^{th} sideband
L	Lattice parameter
i	Imaginary unit
I	Current
G	Conductance
s_n	Sign of n^{th} energy band
s'_n	Sign of n^{th} energy band inside the barrier
e	Electron charge
V_{LR}	Voltage across the sample

ω	AC driving frequency
J_n	n^{th} order Bessel function of the first kind
S	Noise
f_α	Fermi distribution in reservoir α
Ω	Response frequency
Re	Real part
Im	Imaginary part
Int	Integer part

Chapter 1

Introduction

In the fast-changing 21st century world with increasingly high rate of information exchange there is a constant demand for improving the performance of electronic devices. With a major section of the computer industry based on Si technology, engineers foresee an end to Moore's downscaling law by 2020's since at that time the needed transistor size will be on atomic scale. Leakages due to quantum tunneling are becoming more evident with the decrease in size of an electronic device. Although this problem does not seem resolvable, engineers are looking for solutions alternative to silicon technology. Their search led us to the carbon - a lighter element of the same periodic table group as silicon. Active research on carbon-based electronics has already been pursued for several decades, starting from the discovery of fullerenes [1], carbon nanotubes [2], and ending a fairly recent experimental extraction of graphene [3]. The latter one has been attracting increasing attention of scientific communities due to a unique combination of properties of the material, interesting from both, device-oriented and fundamental science, points of view. The intention of this project is to examine the possibility of utilizing graphene in high-mobility transistors for high-frequency applications [4, 5, 6]. This chapter contains an overview of the field. At the end of it, we explain the motivation and targets set for this thesis, and outline its structure.

1.1 Graphene overview

So what is so intriguing about graphene? First of all, it is a one-atom thick two-dimensional layer of carbon atoms. Conventional graphite consists of graphene layers weakly bound to each other by interplanar forces. These weak bounds are responsible for the fact, that pencils can be used for writing: small flakes of carbon layers are left on a paper when we scratch it against the writing surface. Even small friction breaks the weak interplanar bonds, however, it is hard to find a single layer of graphene in pencil writings. Nevertheless, almost the same principle lies in the base of a groundbreaking experimental work by Manchester group [3].

1.1.1 Early studies and discovery

Theoretical studies concerning graphene, which is a single layer of graphite, started long before its experimental extraction [7]. Despite the studies ongoing from 1947, the term itself, ”graphene” was introduced much later - in 1987 [8]. The existence of a separable graphene sheet has been a question of scientific debates for a long time [9, 10, 11]. The question was finally resolved in 2004 by Andre Geim, Kostya Novoselov and colleagues who were able to extract graphene from bulk graphite [3].

1.1.2 Fabrication and applications

Currently there are several methods of producing single graphene sheets. The most common ones are exfoliation of graphite[3], epitaxial growth on silicon carbide[12] and chemical vapor deposition on metal substrates[13]. The first technique uses mechanical separation of graphite layers using adhesive materials. As discussed above, it uses the weakness of interplanar bonds in graphite to break it into individual layers. The technique has evolved over time, and now samples large enough to be visible by a naked eye can be produced.

In the second method, SiC substrate is heated up until it is reduced to graphene. The advantage is that formed epitaxial layer of graphene can be processed using techniques developed for Si-based electronics.

The scaling up of graphene production lead to price reduction, thus scientists started to talk about real applications of this novel material. To name a few, it is thought to be a promising candidate for IC circuits due to high carrier mobility [14], or various applications in photovoltaics due to high optical transparency [15]. It can be already used in metrology due to exhibited quantum Hall effect [16, 17], now giving the resistance standard with the same precision as GaAs heterostructures used before. As we can see, the potential application range is quite wide, but in this work we are going to examine how good it is to use graphene in a transistor.

1.1.3 Properties

Two-dimensional crystal lattice of graphene is a hexagonal tiling, commonly named ”honeycomb”. It is known that the reciprocal lattice of it is also hexagonal. Three out of four valence electrons of C are in sp^2 hybridization, the remaining one is in 2p$_z$. The nearest neighbor distance in the cell is 0.142 nm. The primitive cell of the crystal has two distinguishable atoms. Therefore, by translation of these atoms one can form two different sublattices. Having two sublattices results in the fact that electrons and holes are described by two-component wavefunctions, referred to as ”pseudospinors”. This is very important for tight binding approach, following which, one can deduce the Hamiltonian for electrons and holes in graphene. In the absence of externally applied fields, it has the following form in low-energy limit:

$$H = -i\hbar v_F \vec{\sigma} \cdot \vec{\nabla}, \tag{1.1}$$

where $v_F \approx 10^6\, ms^{-1}$ denotes Fermi velocity, $\vec{\sigma} = (\sigma_x, \sigma_y)$ is a two-dimensional vector containing Pauli matrices, and $\vec{\nabla}$ is a two-dimensional vector differentiation operator. The energy dispersion relation obtained from (1.1) has the form $E = \hbar v_F |k|$[7]. By examining this relation one can find, that it is linear in k and contains no dependence on particle mass, unlike other 2DEG systems. Such dispersion relation is characteristic for massless photons and ultrarelativistic particles, and neutrino. The Fermi velocity plays here a role of the speed of light. However, in contrast to e.g. photons, electrons and holes in graphene are fermions, making them the unique particles discovered so far with such combined properties. They are commonly referred to as Dirac fermions, while the six corners of Brillouin zone are called Dirac points. At these points, the conduction band touches the valence band, thus making graphene a zero-gap semiconductor. We will examine detailed properties of graphene further in this work.

1.2 Motivation and goals

It has been argued by various authors [6, 18] that outstanding properties of graphene are suitable for RF communication applications. High Fermi velocity of the carriers in graphene allows them to respond quickly to externally applied electrical fields making the material a great candidate for high-frequency FET applications. In addition, one-atom thick channel is so far the smallest electronics can get, and graphene is exactly one-atom thick plane. The author was fascinated by potential applications of graphene in this field, and this served as a motivation for the conducted thesis work.

The attempt here is to develop a working model for a four-terminal transistor based on a single graphene layer. Thesis goals are to examine current and noise responses to DC and AC drives applied to the top gate in such a device, to demonstrate the fundamental differences in physics, and, therefore, operation, of it in comparison to traditional FET structures based on semiconductors.

1.3 Thesis structure

In Chapter 2 we concentrate on basic properties of graphene, derive Dirac Hamiltonian from tight binding model and explore the resulting linear dispersion relation. In connection with relativistic behavior of the system we derive an expression for probability current density.

In Chapter 3 the author introduces most of the concepts and mathematical tools used in the work. We start out considering a general structure of a device of interest, from classical point of view. Then we consider the underlying mechanism of its operation. In order to do that we solve the tunneling through a potential barrier problem. Next, the key differences between Schrödinger and Dirac (graphene) systems are explained. A scattering matrix method is introduced in connection with a many-channel transport problem. In the middle of the chapter we introduce an operator approach needed for conductance calculation. Then we proceed to the calculation of the conductance itself, investigating its behavior for the case of static barrier in graphene and 2DEG. Landauer approach to the scattering problem is examined in details. In the second half of the chapter, the author considers time-dependent transport. First, Tien-Gordon approach is introduced in order to solve time-dependent Schrödinger equation. By using this approach, we obtain the corrections to static conductance resulting from AC-driven potential barrier in graphene.

Chapter 4 concentrates on computation of noise. The author starts with a general operator approach for the static case. Once a general expression for noise is obtained, the author computes zero-frequency noise. The chapter ends with a discussion on Fano factor and comparison to other graphene-based systems.

In the final Chapter 5 we summarize the obtained results, draw conclusions from the presented work and present the outlook for the possibilities of expansion and improvement on the basis of presented work.

Chapter 2

Graphene as a relativistic material

In this chapter we examine some of the basic properties of graphene. We show how the symmetry of the crystal lattice results in peculiar properties of this material. We introduce pseudospinors, and obtain the Hamiltonian for the system, and discuss the resulting dispersion relation. The Hamiltonian is derived from a tight-binding model, here we follow the steps provided in [19]. The last section of the chapter contains a derivation of the probability current density in graphene and its connection to relativistic materials.

2.1 Tight binding model

We start with the symmetry of graphene's unit cell. If one attempts to construct a Wigner-Seitz primitive cell around an atom in graphene one finds that it's not enough to cover all the atoms, and there is another lattice of Wigner-Seitz cells similar to the constructed, but shifted and rotated 180 degrees with respect to the original, and together they fill the entire plane. From this we conclude that graphene has two inequivalent triangular sublattices, or, in other words, the unit cell of graphene consists of two inequivalent atoms. Visualisation of the concept is presented in Fig. 2.1.

Now one can view the wavefunction of a charge carrier in graphene as a superposition of the wavefuctions from two sublattices, call them A and B:

$$\psi_k(r) = A_k \psi_k^A(r) + B_k \psi_k^B(r), \tag{2.1}$$

where A and B are some complex coefficients dependent on quasimomentum

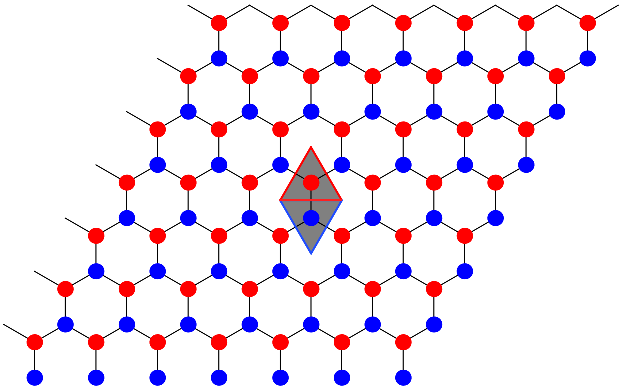

Figure 2.1: Two inequivalent sublattices in graphene. Simple Wigner-Seitz cells are shown as red(blue) triangles for corresponding sublattices. Together they form a unit cell - grey-filled.

$\vec{k}$. The sublattice wavefunctions, in turn, are:

$$\psi_k^\alpha = \sum_{R_l} e^{i\vec{k}\cdot\vec{R}_l}\phi^\alpha(\vec{r}+\vec{\delta}_\alpha+\vec{R}_l), \quad \alpha = A, B, \tag{2.2}$$

having a form of Bloch functions with ϕ being atomic wave functions, R_l being atomic position in the constructed lattice, δ_α a vector connecting R_l's with α's position in the unit cell. For example, we can choose $\delta_A = 0$.

Now we are ready to write the time-independent Schrödinger equation for our system:

$$H\psi_k(r) = E_k\psi_k(r), \text{ with } \psi_k = \begin{pmatrix} A_k & B_k \end{pmatrix}\begin{pmatrix} \psi_k^A \\ \psi_k^B \end{pmatrix} \tag{2.3}$$

By multiplying each side of the last equation with $\psi_k^*(r)$ and integrating over space (r) we can arrive at the following form, avoiding k index and integral for the matter of convenience:

$$\begin{pmatrix} A^* & B^* \end{pmatrix}\begin{pmatrix} \psi_A^* H\psi_A & \psi_A^* H\psi_B \\ \psi_B^* H\psi_A & \psi_B^* H\psi_B \end{pmatrix}\begin{pmatrix} A \\ B \end{pmatrix} = E\begin{pmatrix} A^* & B^* \end{pmatrix}\begin{pmatrix} \psi_A^*\psi_A & \psi_A^*\psi_B \\ \psi_B^*\psi_A & \psi_B^*\psi_B \end{pmatrix}\begin{pmatrix} A \\ B \end{pmatrix} \tag{2.4}$$

At this point we have to make some assumptions in order to simplify the problem. First of all, we neglect the overlap between wavefunctions of neighbouring sublattices $\int d^3r\, \psi_A^*\psi_B = \int d^3r\, \psi_B^*\psi_A = 0$. Next we assume chemical equivalence of two sublattices, thus getting $\psi_A^* H\psi_A = \psi_B^* H\psi_B$.

Then we can put these terms to zero, since they are contributing a constant shift to the energy. We also note that $\int \mathrm{d}^3r\, \psi_A^* \psi_A = \int \mathrm{d}^3r\, \psi_B^* \psi_B = N$ is the number of unit cells in the system. We describe the hopping term $H^{AB} = \int \mathrm{d}^3r\, \psi_A^* H \psi_B = N t^{AB}$ with

$$t_k^{AB} = \sum_{\vec{R}_l} e^{i\vec{k}\cdot\vec{R}_l} \int d^2r \phi_A^*(\vec{r} - \vec{R}_k) H \phi_B(\vec{r} + \vec{\delta}_{AB} - \vec{R}_m) \tag{2.5}$$

Due to honeycomb geometry of graphene it is enough to consider hopping of electrons to the nearest sites, which are three, and they all lie in another sublattice. The next nearest neighbours lie $\sqrt{3}$ times further. So (2.5) simplifies to:

$$t_k^{AB} = t(1 + e^{-i\mathbf{k}\cdot\mathbf{L_2}} + e^{-i\mathbf{k}\cdot\mathbf{L_3}}), \quad t = \int d^2r \phi_A^*(\vec{r}) H \phi_B(\vec{r} + \vec{\delta}_{AB}), \tag{2.6}$$

where $\mathbf{L_{2,3}} = \frac{\sqrt{3}L}{2}(\pm\hat{x} + \sqrt{3}\hat{y})$ are vectors to the nearest neighbours, $L = 0.142$ nm is C-C bond length. With this transformation (2.4) becomes:

$$\begin{pmatrix} A^* & B^* \end{pmatrix} \begin{pmatrix} 0 & Nt_{AB} \\ Nt_{BA} & 0 \end{pmatrix} \begin{pmatrix} A \\ B \end{pmatrix} = E \begin{pmatrix} A^* & B^* \end{pmatrix} \begin{pmatrix} N & 0 \\ 0 & N \end{pmatrix} \begin{pmatrix} A \\ B \end{pmatrix} \tag{2.7}$$

Now it's straightforward to solve, giving $|E|^2 = t_{AB} t_{BA}$. From the form of (2.6) one can easily get $t_{AB} = t_{BA}^*$, so $E = \pm|t_{BA}|$. One can notice that for some values of quasimomentum the interatomic overlap energy t_k^{AB} vanishes, namely at:

$$\pm\mathbf{K} = \pm\frac{4\pi}{3\sqrt{3}L}\hat{x} \tag{2.8}$$

We can see, that the conduction band ($E > 0$) touches the valence band ($E < 0$) at these K and K' points, which are actually corners of the first Brillouin zone. Analogically to the crystal lattice, for which we had two inequivalent types of atoms, here we get two inequivalent points K and K' in the reciprocal space. Since carbon atoms have four electrons each, and three of the electrons are used in formation of σ-bonds, one π-electron per atom is left. But each π-orbital can accommodate two electrons due to spin degeneracy, so it is just half-filled. Therefore, the Fermi energy of undoped graphene lies exactly at K and K' points - at zero energy level (Fig. 2.2).

2.2 Dirac Hamiltonian

Now we can take a closer look at these points. Since $E = 0$ exactly at them we can expand (2.6) for low energies, or, equivalently, low momentum κ with

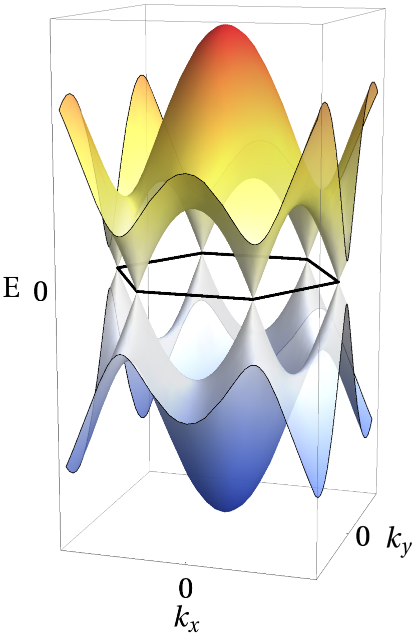

Figure 2.2: Energy bands of graphene. The edges of the first Brillouin zone are shown with solid black line. Corners are K and K' points, where conduction ($E \geq 0$) and valence ($E \leq 0$) bands touch each other.

respect to the points K and K': $\mathbf{k} = \pm\mathbf{K} + \boldsymbol{\kappa}$, $\kappa \ll K$, giving us:

$$\begin{aligned} t^{AB}_{\pm\boldsymbol{K}+\boldsymbol{\kappa}} &= t\left(1 + e^{-i(\pm\boldsymbol{K}+\boldsymbol{\kappa})\cdot\boldsymbol{a_2}} + e^{-i(\pm\boldsymbol{K}+\boldsymbol{\kappa})\cdot\boldsymbol{a_3}}\right) \approx \\ &\approx t\left(1 + (1 - \boldsymbol{\kappa}\cdot\boldsymbol{a_2})\, e^{\mp i\frac{2\pi}{3}} + (1 - \boldsymbol{\kappa}\cdot\boldsymbol{a_3})\, e^{\pm i\frac{2\pi}{3}}\right) = \tfrac{3at}{2}(\pm\kappa_x - i\kappa_y) \end{aligned} \tag{2.9}$$

Now we can plug the obtained expression into the energy eigenvalues or directly into the Hamiltonian reading:

$$H_{\pm} = \begin{pmatrix} 0 & t^{\pm}_{AB} \\ t^{\pm}_{BA} & 0 \end{pmatrix} = \tfrac{3at}{2}\begin{pmatrix} 0 & \pm\kappa_x - i\kappa_y \\ \pm\kappa_x + i\kappa_y & 0 \end{pmatrix} \tag{2.10}$$

Recalling that $\boldsymbol{\kappa} = -i\boldsymbol{\nabla}$ one easily arrives at the following expression:

$$H_{+} = -i\hbar v_f(\boldsymbol{\sigma}\cdot\boldsymbol{\nabla}), \quad H_{-} = i\hbar v_f(\boldsymbol{\sigma}^{*}\cdot\boldsymbol{\nabla}), \tag{2.11}$$

where $\boldsymbol{\sigma} = \begin{pmatrix} \sigma_x \\ \sigma_y \end{pmatrix}$ is the Pauli matrix vector in two dimensions, we defined Fermi velocity in graphene $v_f = \frac{3tL}{2\hbar}$. Knowing the interatomic overlap energy t to be around 3 eV, we estimate $v_f \approx 10^6 m/s$. The overlap energy to the second-nearest neighbours is smaller than 0.6 eV, and third-nearest neighbours around 0.1 eV, based on *ab initio* calculations [23]. One can easily see that low-energy dispersion relation $E = \pm\hbar|k|v_f$ is linear in momentum and does not depend on electron mass. It can be seen in Fig. 2.2 as cones emerging from K points. This type of dispersion relation is characteristic for relativistic particles, although here the role of speed of light is played by Fermi velocity. The Hamiltonian (2.11), spectrum, and points K, all bear the name of Paul Dirac.

We can note, that the approximations being made are in fact bringing us to the mesoscopic scale. We have to assume that electron's wavelength is larger than C-C bond length, so that we are treating graphene as a continuum medium. Nevertheless, the contributions from the sublattices are still distinguishable. Thus, we understand this as an internal degree of freedom, namely chirality since it is similar in mathematical description to chirality of spin, but here it is due to pseudospinors.

Another important remark to be put here is that despite the fact that we have obtained Hamiltonians for K and K' valleys seemingly separately from each other, we have assumed that they are decoupled. In the most general case of intervalley scattering, we have to deal with a four-by-four Hamiltonian matrix and the spinors have four components. Here we already assumed that spin degree of freedom does not influence the scattering mechanism in this setup. So what does the assumption about non-intermixing valleys mean? We have to assume that the potential cannot scatter the paticles by a large enough wavevector to bring them from one K valley to another. Since this is done in k-space, in real space it would mean that the potential is smooth on the atomic scale thus covering both types of sublattices. In addition, our sample of graphene should be inifinite on mesoscopic scale since the quantization due to standing waves can mix the valleys together.

2.3 Probability current density

Since eventually we want to compute current through our system, and it is closely related to the probability current density, it is useful to obtain an expression for the latter. Traditional probability current density in quantum mechanics is obtained from Schrödinger equation, and has the following form:

$$\vec{j} = \frac{\hbar}{2mi}\left(\Psi^* \boldsymbol{\nabla} \Psi - \Psi \boldsymbol{\nabla} \Psi^*\right) \tag{2.12}$$

Recalling the results of the previous section, we have massless charge carriers in graphene along with pseudospinor form of the wavefunctions. Clearly, the traditional form must be modified for this case, let us derive an expression suitable for graphene.

We start with Dirac equation for valley K (2.11). Assume we apply some external potential $V = V(r,t)$ having some matrix form:

$$i\hbar\frac{\partial}{\partial t}\Psi = -i\hbar v_f\left(\boldsymbol{\sigma}\cdot\boldsymbol{\nabla} + V\right)\Psi, \tag{2.13}$$

where $\Psi = \begin{pmatrix}\Psi_A \\ \Psi_B\end{pmatrix}$. Now we take its Hermitian conjugate:

$$-i\hbar\frac{\partial}{\partial t}\Psi^\dagger = i\hbar v_f\left(\boldsymbol{\sigma}\cdot\boldsymbol{\nabla} + V\right)\Psi^\dagger \tag{2.14}$$

Note that $\sigma\cdot\nabla$ is Hermitian, making the Hamiltonian of a singe valley anti-Hermitian. Here we also require the matrix of potential to be Hermitian. Now we multiply (2.13) with $\Psi^\dagger$ on the left, and (2.14) with Ψ on the right, and subtract them, giving us:

$$\left(\left(\frac{\partial}{\partial t}\Psi^\dagger\right)\Psi + \Psi^\dagger\frac{\partial}{\partial t}\Psi\right) = -v_f\left(\Psi^\dagger\left(\boldsymbol{\sigma}\cdot\boldsymbol{\nabla}\Psi\right) + \left(\boldsymbol{\sigma}\cdot\boldsymbol{\nabla}\Psi^\dagger\right)\Psi\right) \tag{2.15}$$

Now on the left-hand side one can recognize the time derivative of the probability density function. But we know from the continuity equation that $\frac{\partial}{\partial t}\left(\Psi^\dagger\Psi\right) + \boldsymbol{\nabla}\cdot\boldsymbol{j} = 0$. From this we can see that:

$$\begin{aligned}\boldsymbol{\nabla}\cdot\boldsymbol{j} &= v_f\left(\Psi^\dagger\left(\boldsymbol{\sigma}\cdot\boldsymbol{\nabla}\Psi\right) + \left(\boldsymbol{\sigma}\cdot\boldsymbol{\nabla}\Psi^\dagger\right)\Psi\right) = \\ &= v_f\boldsymbol{\nabla}\cdot\begin{pmatrix}\Psi_A^\dagger\Psi_B + \Psi_B^\dagger\Psi_A \\ i\Psi_B^\dagger\Psi_A - i\Psi_A^\dagger\Psi_B\end{pmatrix}\end{aligned} \tag{2.16}$$

Now we can write down the final expression for probability current density:

$$\vec{j} = v_f\begin{pmatrix}\Psi_A^\dagger\Psi_B + \Psi_B^\dagger\Psi_A \\ i\Psi_B^\dagger\Psi_A - i\Psi_A^\dagger\Psi_B\end{pmatrix} = v_f\begin{pmatrix}\Psi^\dagger\sigma_x\Psi \\ \Psi^\dagger\sigma_y\Psi\end{pmatrix} = v_f\Psi^\dagger\vec{\sigma}\Psi \tag{2.17}$$

Analogically, for valley K' we can find the probability current density to be:

$$\vec{j}' = -v_f\Psi^\dagger\vec{\sigma}^*\Psi \tag{2.18}$$

Having this figured out we can proceed to the main part of the thesis.

Chapter 3

Current calculation

The key point in derivation of current behavior of the system is to understand the underlying scattering process. Thus, having Dirac Hamiltonian at our disposal, we now can proceed to solving a problem of tunneling through the barrier.

The derived probability current density will serve us in finalizing current computation. We are going to examine the system in both, DC and AC driving regimes. We introduce scattering matrix approach, which is of particular use for multi-channel scattering encountered in AC response. Finally we describe an operator approach following Landauer-Büttiker theory [26, 25] obtaining an expression for the current through the system.

In connection with the barrier tunneling, we also introduce 2DEG computation. It is of particular interest in here, since 2DEG can be obtained in conventional transistors, thus we can compare the behavior of 2DEG- and graphene-based devices.

3.1 Device operating principles

Here we explain the basic structure of a graphene-based FET and the roles of different parameters which enter the theoretical model developed in the next chapters.

The schematics of the transistor is presented in Fig. 3.1. It has four active terminals. Two contacts are used effectively to inject and capture electrons from graphene, and work as reservoirs in the proposed problem. These are source and drain. Another two contacts are used to control graphene itself - a back gate electrode moves the Fermi level of the entire graphene sheet, while a top gate applies an external potential to a small region in the

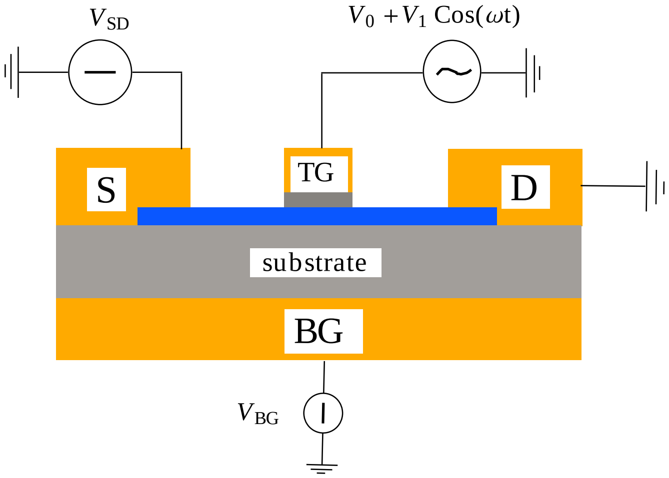

Figure 3.1: Schematics of the transistor. S=source, D=drain, BG=back gate, TG=top gate

center of the sheet. It will move the Fermi level only in this selected region, and will be overimposed on the effect introduced by a back gate. In this way we are able to introduce a potential barrier in graphene region under the top gate with respect to other parts of the sample. Since the top and back gates are separated from graphene by insulating substrate layers, they do not have a direct effect on the transport, like introducing charge carriers as source and drain do, but rather only in creating an effective potential landscape. In this work we apply a potential of V_{SD} across the sample which will initiate charge transfer between source and drain. Back gate potential V_{BG} is tuned in such a way, that it brings the Fermi level in graphene close to the Dirac point. The top gate can deliver a static drive of amplitude V_0 and a periodic potential with strength V and frequency ω on top of the static part.

Now we assume a setup where the source and drain are sufficiently far away from each other and the top gate so that the electron current is realized only by propagating waves, we assume no evanescent wave coupling between the electrodes. Now once we have propagating waves in our graphene sample, we can proceed to the fundamental quantum level of the system and examine the scattering process in the region around the top gate and how it influences the current and noise characteristics of the device, which is described in the following sections.

3.2 Static drive

Under this section we are going to examine the system under an external potential, which does not change in time.

3.2.1 1D and 2D rectangular potential barriers

Here we start out with a basic quantum mechanical problem - tunneling through a potential barrier.

We examine the case of material with Schrödinger type behavior first. Consider a rectangular barrier in such a system:

$$-\frac{\hbar^2}{2m}\nabla^2\Psi(\vec{r},t)+V(\vec{r})\Psi(\vec{r},t)=i\hbar\frac{\partial}{\partial t}\Psi(\vec{r},t) \tag{3.1}$$

In the simplest case, we are in one dimension. External potential is constant $V = V_0$ inside the barrier, while being zero elsewhere. The solutions to the equation are plane waves, having the form of $\Psi(x,k,t) = \psi(x)e^{-iEt/\hbar}$ with $\psi(x)$ being different for each part of the barrier in Fig. 3.2:

$$\begin{aligned}\psi_I(x) &= e^{ikx} + r_0e^{-ikx}\\ \psi_{II}(x) &= a_0e^{iqx} + b_0e^{-iqx}\\ \psi_{III}(x)) &= t_0e^{ikx}\end{aligned} \tag{3.2}$$

Here we already rescale all the amplitudes with respect to the incident wave, whose amplitude is set to unity. In this material we have quadratic dispersion relation giving $k = \frac{\sqrt{2mE}}{\hbar}, q = \frac{\sqrt{2m(E-V_0)}}{\hbar}$.

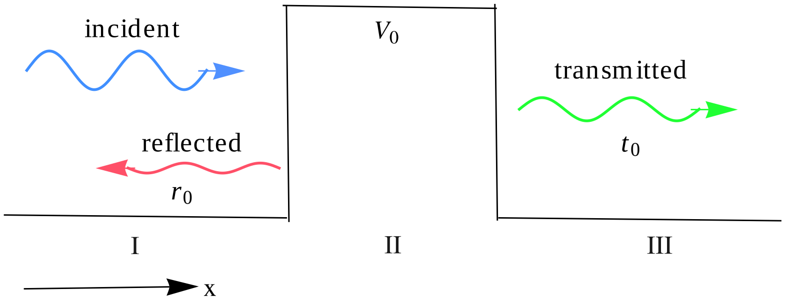

Figure 3.2: 1D potential barrier

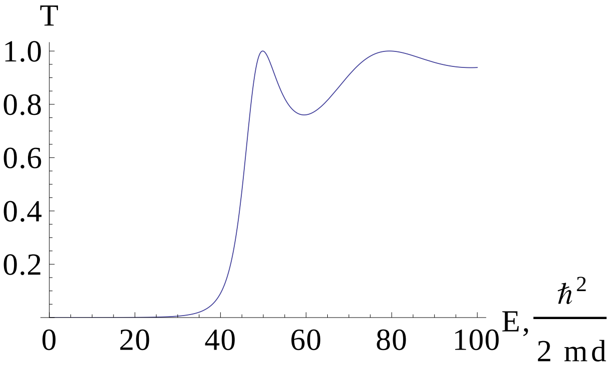

Figure 3.3: Transmission through an arbitrary rectangular barrier. $V_0 = 40\frac{\hbar^2}{2md}$

By matching different region solutions at the boundaries between them, we get a set of equations to solve. In Schrödinger material we require both, wavefunction and its spacial derivative, to be continuous, giving us four boundary conditions:

$$\begin{array}{l} \psi_I(0) = \psi_{II}(0) \\ \psi_I'(0) = \psi_{II}'(0) \\ \psi_{II}(D) = \psi_{III}(D) \\ \psi_{II}'(D) = \psi_{III}'(D) \end{array} \tag{3.3}$$

After solving this set of equations we get [20]:

$$t_0 = \frac{4kqe^{i(q-k)D}}{(k+q)^2-(k-q)^2e^{2iqD}}; \quad r_0 = \frac{(k^2-q^2)\sin qD}{2ikq\cos qD+(k^2+q^2)\sin qD} \tag{3.4}$$

Transmission probability $T = |t_0|^2$ through a rectangular 1D barrier is shown in Fig. 3.3. We can see that the interference inside the barrier may result in an enhancement or reduction of transmission through the barrier. Naturally, the inteference depends on the width of the barrier and the energy of the particle - in expression (3.4) it is the exponential term in the denominator resulting from the interference.

For two-dimensional(2D) barriers, with infinite width in one of the dimensions, we can use the specular reflection, which states that the momentum component parallel to the barrier is conserved. It is an assumption, but it can be fulfilled, since it basically requires the wavelength of the particle to be larger than the features of the barrier. Then, the barrier itself will appear as a continuous medium without sharp edges. Sharpness of the material becomes apparent only on atomic scale, so we simply need $\lambda \gg 0.1$

nm. Large wavelength corresponds to low-energy particles. And in this work, low-energy excitations are exactly what we are interested in, at least in graphene. With the transverse momentum conserved, the situation can be again simplified to 1D, and the transmission amplitude has exactly the same form as in (3.4)

$$t_0 = \frac{4k_x q_x e^{i(q_x - k_x)D}}{(k_x + q_x)^2 - (k_x - q_x)^2 e^{2iq_x D}}, \tag{3.5}$$

only now the projections along the x-axis perpendicular to the barrier are taken. The corresponding figure for a 2D barrier will also have angular dependence, as shown in figure 3.4. Here we can see that the considered Schrödinger material does not posess any particularly interesting transmission dependence on angles. As predicted by analytical formula, 2D case simply follows 1D example. The only difference is that since the projection on x axis is playing the main role, all of the features in the plot are getting elongated for larger angles in comparison to $\phi = 0$. Now we will derive cor-

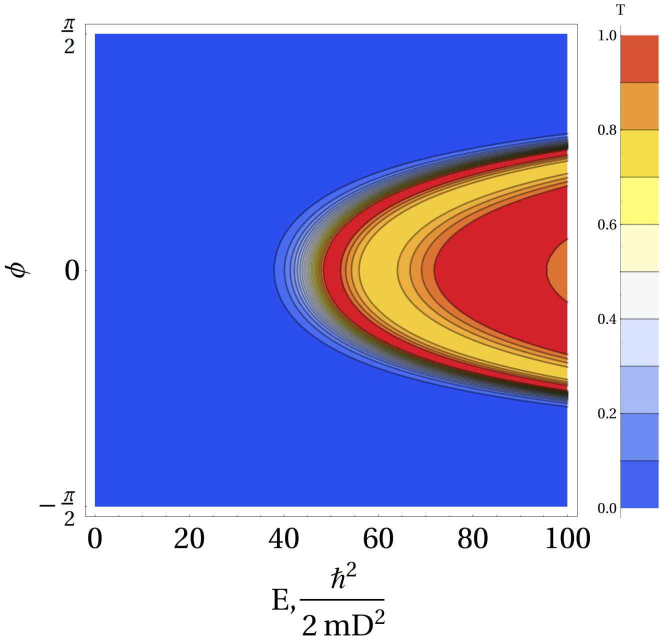

Figure 3.4: Transmission through a 2D rectangular barrier. $V_0 = 40\frac{\hbar^2}{2md}$

responding expressions for graphene-based barriers and compare it to the case examined here.

3.2.2 Graphene and Klein tunneling

Now let us switch to the system of interest. One of the interesting properties of graphene that has been observed falls into the scope of this work. It is called Klein tunneling. A quasi-1D potential barrier of arbitrary width described above can appear absolutely transparent for charge carriers in graphene under special conditions.

Let us consider a case similar to the one described above, but now, since we have graphene instead of a conventional Schrödinger type material, the system is governed by Dirac Hamiltonian (2.11). We can repeat the steps of the previous chapter, and will find out several things. We need to match only the wavefunctions of particles at the boundaries, not their derivatives. Secondly, every wavefunction has a form of a two-component spinor, thus giving us two matching equations. Afterall, we will arrive at the system of four equations, just as in the previous case. Solving it for the transmission coefficient is straightforward, and gives [21]:

$$T = \frac{\cos\phi}{1 - \cos^2(q_x D)\sin^2\phi}, \tag{3.6}$$

where ϕ is the angle of incidence onto the barrier, q_x is the wavevector component along the direction of wave propagation inside the barrier, D is the width of the barrier. Here, we consider the case $E \ll V_0$. The result is visualized in figure 3.5.

By a simple comparison of (3.5) and (3.6) we can see that the Dirac case is very different from standard Schrödinger behavior. Observe from (3.6) that for an incident wave with $\phi = 0$ (perpendicular to the barrier) the fraction on the right-hand side turns to 1, independent of D or q_x. Thus the barrier becomes absolutely transparent for waves incident normally onto it. This phenomenon is commonly known as Klein tunneling. It can be understood physically by recalling pseudospinors: an incident electron-like state can scatter into a hole-like state moving in the same direction inside the barrier and again become an electron-like state after passing it. A more detailed discussion on it is provided in Section 3.3.

Another difference connected with it is that the pattern exhibited in the transmission function continues for all energies, and negative energies correspond to hole-like carriers. In Schrödinger case, however, having negative

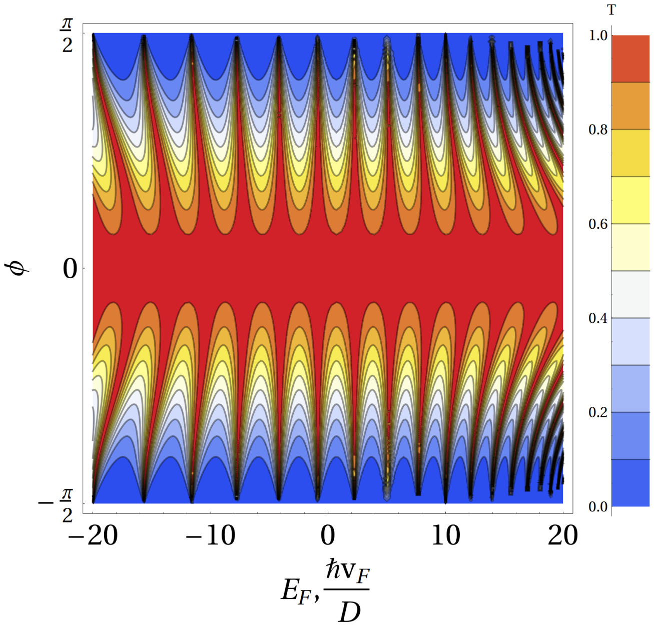

Figure 3.5: Transmission through a rectangular barrier in graphene. $V_0 = 40\frac{\hbar v_F}{d}$

energy corresponds to evanescent waves, and thus there was no transmission for $E < 0$.

Finally, comparing the relative scales we are using in the plots of transmission probabilities, we find that for 2DEG they are connected with the mass of electrons $\frac{\hbar^2}{2md^2}$, while for graphene we consider massless relativistic charge carriers resulting in a natural scale of $\frac{\hbar v_F}{d}$. Judging from this the naive guess is that the size of characteristic features in transmission through 2DEG barrier is much more dependent on the width of the barrier than that of graphene.

A feature common to both types of material is the interference that plays a role in positioning of unity transmission peaks. In both it results in a product of the form $q_x D$. In the case of graphene, these are fringes of peak transmission, which are still superimposed on Klein tunneling picture.

3.2.3 Scattering matrix approach

In previous chapters we considered idealized and very simplified systems. In a more generalized model, the barrier we were considering is in a so-called scattering region, connecting, in our case, source and drain of a transistor. Depending on geometry, impurities and other factors, this region can allow only certain energy levels or paths for particles to have. Thus, the transfer of electrons from one contact to another, from now on called reservoirs, will heavily depend on these factors. Let us call the allowed modes in the scattering region transport channels.

In such a system it is useful to introduce scattering matrix approach. The wavefunction describing charge carriers on either side of the barrier can be described as a superposition of waves travelling to the left or to the right. As we saw in the previous chapter, they are related via boundary matching conditions. These give us a set of equations, which can be solved with the aid of linear algebra in the following form:

$$\begin{pmatrix} A_{Ll} \\ A_{Rr} \end{pmatrix} = \hat{s} \begin{pmatrix} A_{Lr} \\ A_{Rl} \end{pmatrix}, \; \hat{s} = \begin{pmatrix} \hat{r}_L & \hat{t}_R \\ \hat{t}_L & \hat{r}_R \end{pmatrix}, \tag{3.7}$$

where $\hat{s}$ denotes the scattering matrix with $\hat{r}_{R,L}, \hat{t}_{R,L}$ denoting reflection and transmission matrices of the right and left reservoir respectively. The scattering matrix relates the amplitudes of waves scattered from the barrier to amplitudes of incident waves. In this model, we assume time-reversal symmetry, giving us $\hat{s} = \hat{s}^T$ and $\hat{t}_{R,L} = \hat{t}^T_{L,R}$ In this notation the transmission probabilities obtained above are written as $T(E) = \mathrm{Tr}[\hat{t}^\dagger \hat{t}]$. Also note that the unitary requirement from the scattering matrix gives us $\mathrm{Tr}[\hat{s}^\dagger \hat{s}] = R(E) + T(E) = 1$, an intuitive result stating the probability conservation.

The system of interest of this thesis has infinite graphene plane on mesoscopic scale, and contains no impurities, therefore there are no discrete channels. Since we consider transport between two reservoirs, the role of transport channels is played by angle of incidence ϕ, and therefore we have a continuum of transport channels. Thus, any summations over transport channels in our case would transform into integrals over the continuum of angles.

3.2.4 Current in operator approach

In order to describe the quantum mechanical system correctly we need to use operators, their expectation values would correspond to the real measured quantities. We can write down a so-called field operator for charge carriers in the following form:

$$\hat{\Psi}_s(r,t) = \frac{1}{4\pi^2} \sum_{\alpha} \int \mathrm{d}k \, \mathrm{d}\phi \, \hat{a}_{\alpha,s}(k,\phi) \Psi_{\alpha,s}(k,\phi,r,t), \tag{3.8}$$

where $\hat{a}_{\alpha,s}(k,\phi,t)$ is the annihilation operator for a charge carrier coming from reservoir α with wavevector $\vec{k} = (k\cos\phi, k\sin\phi)$ and spin s. We can see that effectively this field operator sums up over the entire k-space thus annihilating any particle at position r. Naturally, its Hermitian conjugate would define a creation field operator at the same point in space-time. The prefactor of $\frac{1}{4\pi^2}$ comes from area renormalization when changing from sum to integration in 2D k-space. Now, using (2.17) we can write down the probability current density operator in valley K as:

$$\hat{\vec{j}}_\alpha = v_f \hat{\Psi}^\dagger_\alpha \vec{\sigma} \hat{\Psi}_\alpha \tag{3.9}$$

To get probability current operator from it, we have to integrate over the cross section of the conductor. Since we are in 2D plane, and want to compute current along x axis, we have to integrate only over y direction:

$$\hat{\vec{P}}_\alpha(t) = \lim_{l\to\infty} \frac{1}{l} \int_0^l \mathrm{d}y \hat{\vec{j}}_\alpha(r,t) \tag{3.10}$$

Now to compute probability current we have to find quantum mechanical average of the probability current operator. For one of the reservoirs:

$$\begin{aligned} \left\langle \hat{\vec{P}}(t) \right\rangle &= \left\langle \lim_{l\to\infty} \tfrac{1}{l} \int_0^l \mathrm{d}y \hat{\vec{j}}(r,t) \right\rangle = \lim_{L\to\infty} \tfrac{1}{l} \int_0^l dy \, v_f \left\langle \hat{\Psi}^\dagger \vec{\sigma} \hat{\Psi} \right\rangle = \\ &= v_f \lim_{l\to\infty} \tfrac{1}{16\pi^4 l} \int_0^l \mathrm{d}y \int \mathrm{d}k \mathrm{d}\phi \mathrm{d}k' \mathrm{d}\phi' \left(\left\langle \hat{a}^\dagger(k,\phi) \hat{a}(k',\phi') \right\rangle \Psi^\dagger_{k,\phi} \boldsymbol{\vec{\sigma}} \Psi_{k',\phi'} \right) \end{aligned} \tag{3.11}$$

But the average in the integrand is nothing else but the average of an occupation number giving us Fermi distribution [22]:

$$\left\langle \hat{a}^\dagger(k,\phi) \hat{a}(k',\phi') \right\rangle = \delta_{\phi\phi'} \delta_{kk'} f(E), \tag{3.12}$$

where $f(E) = \frac{1}{e^{(E-\mu)/k_B\Theta}+1}$ is the Fermi distribution. When transforming from discrete spectrum to continuous $\sum\limits_k \to \int\limits_k$ the delta function is renormalized $\delta_{kk'} \to 2\pi\delta(k-k')$. Plugging this result back into (3.11) we get:

$$\left\langle \hat{\vec{P}}(t) \right\rangle = \tfrac{v_f}{4\pi^2} \lim_{l\to\infty} \tfrac{1}{l} \int\limits_0^l \mathrm{d}y \int \mathrm{d}k\mathrm{d}\phi \left(f(E)\Psi^\dagger_{k,\phi} \boldsymbol{\vec{\sigma}} \Psi_{k,\phi} \right) \tag{3.13}$$

For the case of static barrier we know that there are no sidebands, and we can drop indices "n" and "m" in (3.32) and (3.33). The integrand in (3.13) then can be easily computed to the left of the barrier:

$$\begin{multline}
f(E)\Psi^\dagger_{k,\phi}\sigma_x\Psi_{k,\phi} = \tfrac{1}{2} f(E) \begin{pmatrix} e^{-ik_xx} + r^*\, e^{ik_xx} & s\left(e^{-ik_xx}e^{-i\phi} - r^*\, e^{ik_xx}e^{i\phi}\right) \end{pmatrix} \times \\
\times\, e^{-ik_yy}e^{iEt/\hbar} \begin{pmatrix} 0 & 1 \\ 1 & 0 \end{pmatrix} \begin{pmatrix} e^{ik_xx} + r\, e^{-ik_xx} \\ s\left(e^{ik_xx}e^{i\phi} - r\, e^{-ik_xx}e^{-i\phi}\right) \end{pmatrix} e^{ik_yy}e^{-iEt/\hbar} = \\
= f(E)\, s\, e^{i\phi}(1 - r^* r) = f(E)\, s\, e^{i\phi}\, T,
\end{multline} \tag{3.14}$$

where T is the probability of transmission through the barrier. The same expression holds to the right of the barrier. The fact that the expression is the same on both sides of the barrier comes actually from the symmetry of the scattering matrix. Now, from Section 3.2.2 we know that $T = \frac{\cos^2\phi}{1-cos^2(q_xD)\sin^2\phi}$ in the limit of high barriers ($|E| < e|V_0|/2$). We can see, that the expression under the integral in (3.13) does not contain any y-dependence, therefore the limit transforms into unity and we are left with the integral over the k-space only:

$$\left\langle \hat{\vec{P}}(t) \right\rangle = \tfrac{v_f}{4\pi^2} \iint \mathrm{d}k\mathrm{d}\phi \left(f(E)T(E)\, s\, e^{i\phi} \right) \tag{3.15}$$

Now this is the final expression for the probability current in the general case. Nevertheless, we still can do further simplifications to this expressions under certain assumptions. They are presented in the following section.

3.2.5 Static conductance in graphene

Now let us calculate the current to the right of the barrier:

$$I_x = e\left\langle \hat{\vec{P}}_x(t) \right\rangle = \frac{e\, v_f}{4\pi^2} \iint \mathrm{d}k\, \mathrm{d}\phi s\, e^{i\phi}\, T(k,\phi)\, f(E(k)) \tag{3.16}$$

Starting from this point, the calculation follows the theory, formulated by Landauer [26]. Integration over angles results in a difference of Fermi functions between left (L) and right (R) reservoirs:

$$I_x = \frac{e}{2\pi h} \int \mathrm{d}E \int\limits_{-\pi/2}^{\pi/2} \mathrm{d}\phi s\, T(E, \phi) \cos\phi \, (f_L(E) - f_R(E)) \tag{3.17}$$

Now, under zero-temperature approximation the difference between Fermi functions effectively becomes a delta-function $\delta(E - E_F)$, reducing the integral over energy to a single point at Fermi level:

$$I_x = \frac{e^2 V_{LR}}{2\pi h} \int\limits_{-\pi/2}^{\pi/2} \mathrm{d}\phi s\, T(E_F, \phi) \cos\phi, \tag{3.18}$$

which is nothing else than the famous Landauer formula. The detailed calculation is given in Appendix A.

This is the final expression for the conductance in x direction. To account for spin and valley degeneracy in graphene we have to multiply this result by a factor of 4, and that would be the measurable conductance. After plugging the expression for $T(E_F, \phi)$ in, we get:

$$G_x = \frac{2e^2}{\pi h} \int\limits_{-\pi/2}^{\pi/2} \mathrm{d}\phi \frac{\cos^3[\phi]}{1 - \cos^2[q_x D] \sin^2[\phi]} \tag{3.19}$$

The behavior of the solutions is illustrated in Fig. 3.6 for a potential barrier of arbitrary width and height, the integration was done numerically. We can see that both, the conductance and transmission are oscillating with a clearly defined period when Fermi energy is close to zero. From the explicit formula it can be found to be $\frac{\pi \hbar v_F}{e D}$. Since the conductance itself is nothing else but an integral over the possible transmission channels, the oscillations of it are fading out for high E_F following the fringes in the transmission picture. Looking at part (b) of the figure, we can notice that for high Fermi energies, the fringes of maximal transmission start to bend towards horizontal axis. Therefore, taking a crossection along the vertical axis, we have a chance of intersecting multiple fringes. As more fringes are intersected, their amplitudes are averaged out under the integration over angles. The conductance finally stabilizes at the conductance quantum. Therefore, we can see, that there is a conductance quantum per each unit width of the graphene sheet. Since from the beginning we had no quantization in the transverse direction, assuming infinitely wide graphene plane, now we see that there

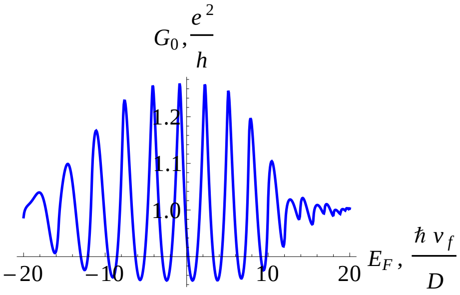

(a) Conductance along the x axis versus Fermi energy

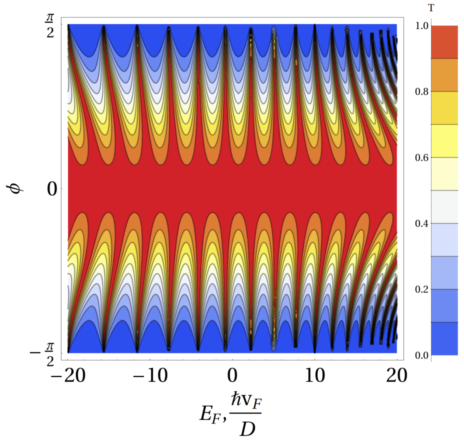

(b) Transmission through the barrier as a function of incidence angle and Fermi energy

Figure 3.6: Conductance and transmission through a barrier of arbitrary width and height. Here $V = 40\frac{\hbar v_f}{D}$.

is an infinite number of channels - each corresponding to one conductance quantum per unit width.

Now, in order to show that such conductance-transmission relation is not something intrinsic to graphene, we examine the case of an analogical system with 2DEG.

3.2.6 Static conductance in 2DEG

In 2DEG the probability current density operator in this case has the following form:

$$\hat{\vec{j}} = \frac{\hbar}{2mi}(\hat{\Psi}^\dagger \vec{\nabla} \hat{\Psi} - \hat{\Psi} \vec{\nabla} \hat{\Psi}^\dagger) \tag{3.20}$$

Denote $A = \Psi^\dagger \nabla_x \Psi - \Psi \nabla_x \Psi^\dagger = 2iTk_x$ on either side of the barrier, it can be easily shown since $R = 1 - T$. Proceeding to the current calculation, repeating the steps done for graphene:

$$\langle \hat{I}_x \rangle = \frac{\hbar e}{2mi(2\pi)^4} \sum_{\alpha,\beta} \int \mathrm{dk d\phi dk' d\phi'} \left\langle \hat{a}^\dagger_\alpha \hat{a}_\beta \Psi^\dagger_\alpha \nabla_x \Psi_\beta - \hat{a}_\alpha \hat{a}^\dagger_\beta \Psi_\alpha \nabla_x \Psi^\dagger_\beta \right\rangle \tag{3.21}$$

We know that $\langle \hat{a}_\alpha \hat{a}^\dagger_\beta \rangle = \langle 1 – \hat{a}^\dagger_\alpha \hat{a}_\beta \rangle = (1 - f_\alpha(E))\delta_{\alpha\beta}\delta(k_\alpha - k_\beta)\delta_{\sigma_\alpha\sigma_\beta}\delta(\phi_\alpha - \phi_\beta)$. Here σ denoted spin. Thus we get:

$$\begin{aligned}
\langle \hat{I}_x \rangle &= \tfrac{\hbar e}{8mi\pi^2} \sum_{\alpha=L,R} \int \mathrm{dkd}\phi (f_\alpha(E) - (1 - f_\alpha(E)))A_\alpha = \\
&= \tfrac{\hbar e}{8mi\pi^2} \sum_{\alpha=L,R} \int \mathrm{dkd}\phi (2f_\alpha(E) - 1) 2iT(k,\phi) k \cos\phi = \\
&= \tfrac{e}{4\pi^2\hbar} \sum_{\alpha=L,R} \int \mathrm{dEd}\phi (2f_\alpha(E) - 1) T(E,\phi) \cos\phi = \\
&= \tfrac{e}{\pi h} \int_{\phi=-\pi/2}^{\pi/2} \mathrm{dEd}\phi (f_L(E) - f_R(E)) T(E,\phi) \cos\phi = \\
&= \tfrac{e^2 V}{\pi h} \int_{\phi=-\pi/2}^{\pi/2} \mathrm{dEd}\phi\, \delta(E - E_F) T(E,\phi) \cos\phi = \frac{e^2 V}{\pi h} \int_{-\pi/2}^{\pi/2} \mathrm{d}\phi\, T(E_F,\phi) \cos\phi
\end{aligned} \tag{3.22}$$

It also has to be multiplied by two accounting for spin degeneracy. This result has the same form as for graphene, and reproduces well-known Landauer formula [26].

The conductance for 2DEG is shown in Fig. 3.7. The figure displays conductance for energies below the barrier height, since it is the traditional region of interest for transistor applications. We can see, that in contrast to graphene, for 2DEG the transmission probability is exponentially decaying with lower energies, resulting in a similar behavior for conductance. Thus, while we can firmly control the magnitude of the conductance with barrier height V_0 in 2DEG, in graphene we do not have such easy control - we can only influence the distance between high-transmission fringes and have no

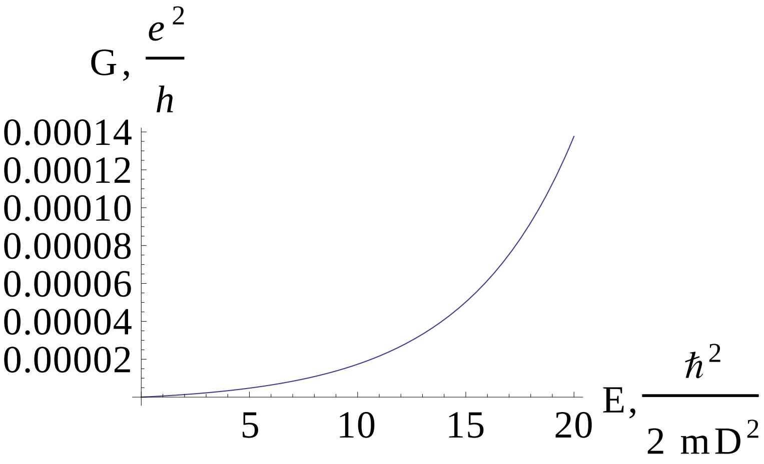

Figure 3.7: Conductance through a barrier $V_0 = 40\frac{\hbar^2}{2mD}$ in 2DEG

control over zero-angle perfect Klein tunneling region. From another point of view, since the conductance in graphene is less sensitive to the height of the barrier - note, in high-barrier approximation - it is better in terms of stability and control - the output will be always around a conductance quantum per unit length.

Now, having the static case for both types of materials analysed, we no longer will discuss the behavior in 2DEG: firstly, because it has been thoroughly examined by various authors before, including Landauer, secondly, because the measured quantities like conductance and noise simply follow the transmission from the scattering process already analysed in here, and transmission picture for 2DEG simply has an exponential dependence for high barriers - not much to discuss in here.

With this in mind, we can proceed to a more complicated problem connected with the graphene transistor - derivation of current response in the presence of an oscillating driving potential.

3.3 AC drive

In this section we modify the existing rectangular static potential barrier by an additional small AC drive. The resulting modification of conductance of the system is examined under various limits and approximations.

3.3.1 Tien-Gordon theory

Since we are going to discuss a time-varying potential we need to see how it influences the form of the solutions to the Schrödinger equation (SE). The theory for this kind of system was pioneered by Tien and Gordon [24]. As we know, for a rectangular barrier time-independent SE looks like:

$$H_0\psi = E\psi, \tag{3.23}$$

where H_0 is the Hamiltonian of the system with the static potential barrier, ψ is the wavefunction and E is energy. The solutions to it are plane waves. Now, once we add an additional AC electric field to the barrier, the Hamiltonian changes to:

$$H = H_0 + eV\cos(\omega t), \tag{3.24}$$

where e is the elementary charge, ω is the frequency of the field, V its amplitude. Thus, SE can be now written as:

$$i\hbar\frac{\partial}{\partial t}\Psi(\vec{r},t) = H\Psi(\vec{r},t) = (E + V\cos(\omega t))\Psi(\vec{r},t) \tag{3.25}$$

Now we can see that the operators themselves do not have a coordinate dependence, thus the wavefunction can be actually separated into spatial and temporal components $\Psi(\vec{r},t) = \psi(\vec{r})\Phi(t)$. The resulting partial differential equation for $\Phi(t)$ can be solved giving:

$$\Phi(t) = \exp[-\frac{i}{\hbar}(Et + \frac{eV}{\omega}\sin\omega t)] \tag{3.26}$$

Now we can Fourier expand it:

$$\Phi(t) = \sum_n c_n \exp[-in\omega t] \tag{3.27}$$

where coefficients c_n are found from inverse Fourier transform:

$$c_n = \frac{1}{2\pi}\int\limits_{-\pi}^{\pi} d(\omega\text{t})\exp[-i(\frac{eV}{\hbar\omega}\sin\omega t - n\omega t)] \tag{3.28}$$

The odd parts will go away under the integration, and the coefficients will be defined as:

$$c_n = \frac{1}{\pi}\int\limits_{0}^{\pi} d(\omega\text{t})\cos[\frac{eV}{\hbar\omega}\sin\omega t - n\omega t] = J_n\left(\frac{eV}{\hbar\omega}\right) \tag{3.29}$$

And as we can see they have the form of Bessel functions. Thus, the solutions to the time-dependent SE have the form:

$$\Psi(r,t) = \psi(r) \sum_{n=-\infty}^{\infty} \left[J_n \left(\frac{eV}{\hbar\omega} \right) \exp\left(-i\left(E + n\hbar\omega\right) t/\hbar\right) \right], \tag{3.30}$$

where J_n is the n^{th}-order Bessel function of the first kind. One can deduce from the form of the solutions that apart from the main energy band E, effective sidebands $E + n\hbar\omega$ are formed. Now, waves incident on the barrier can scatter into different energy states, thus instead of having one transmission channel, we have many. Naturally, the overall transmission through such barrier is the sum over all single channel transmissions. The advantage of this theory is that it applies equally well to both, Schrödinger and Dirac particles. Therefore, now we can proceed and examine the AC driving of graphene.

3.3.2 Scattering in graphene

Scattering problem

Now let us consider a 2D rectangular barrier in graphene infinitely wide in y-direction. With additional oscillating potential applied:

$$H = H_0 + eV\cos(\omega t), \tag{3.31}$$

where $H_0 = -i\hbar v_f \boldsymbol{\sigma} \cdot \boldsymbol{\nabla} + eV_0$ is the time-independent Hamiltonian in the absence of AC field. Here we asssume V has a form of the identity matrix $V = \begin{pmatrix} V & 0 \\ 0 & V \end{pmatrix}$. In region II (Fig. 3.8) due to Tien-Gordon effect energy sidebands are formed. Thus, for the wave with energy E, incident from the left, we have:

$$\begin{aligned}
\Psi_i(x,y,t) &= \tfrac{1}{\sqrt{2}} \sum_{n=-\infty}^{\infty} \left[\delta_{n0} \begin{pmatrix} 1 \\ \eta_n \end{pmatrix} e^{ik_x^{(n)}x} e^{ik_y y} e^{-iEt/\hbar} \right] \\
\Psi_r(x,y,t) &= \tfrac{1}{\sqrt{2}} \sum_{n=-\infty}^{\infty} \left[r_n \begin{pmatrix} 1 \\ \bar{\eta}_n \end{pmatrix} e^{-ik_x^{(n)}x} e^{ik_y y} e^{-i(E+n\hbar\omega)t/\hbar} \right] \\
\Psi_t(x,y,t) &= \tfrac{1}{\sqrt{2}} \sum_{n=-\infty}^{\infty} \left[t_n \begin{pmatrix} 1 \\ \eta_n \end{pmatrix} e^{ik_x^{(n)}(x-D)} e^{ik_y y} e^{-i(E+n\hbar\omega)t/\hbar} \right]
\end{aligned} \tag{3.32}$$

Factor of $\frac{1}{\sqrt{2}}$ in front of the expressions for Ψ comes from pseudospinor normalization condition. Here δ_{n0} is Kronecker delta function, $\eta_n = s_n \frac{k_x^{(n)} + ik_y}{|k_n|}$

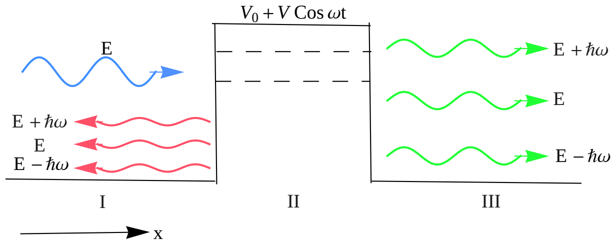

(a) Side view of the barrier. The incoming wave at the main energy band E is scattered into multiple sidebands $E \pm \hbar\omega$

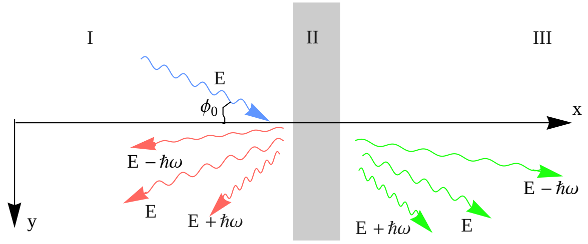

(b) Top view of the barrier. It is infinitely wide along y direction. An incoming wave at angle ϕ_0 is scattered into multiple at different angles

Figure 3.8: Barrier with oscillating potential

and $\bar{\eta}_n = s_n \frac{-k_x^{(n)} + ik_y}{|k_n|}$, with $|k_n| = \sqrt{(k_x^{(n)})^2 + k_y^2}$. $s_n = sign(E + n\hbar\omega)$ is the sign of an energy band. It is of particular interest, since it implies which type of carrier we are dealing with, and the incident electron can be reflected into a hole at different energy band.

Thus, in region I we have $\Psi_I = \Psi_i + \Psi_r$. The reflected wave scatters from the barrier, which has multiple sidebands, thus the reflected wave is a superposition of scattered waves from different energy bands. The transmitted wave is affected in a similar way. In region II the wave has Tien-Gordon form:

$$\begin{aligned} \Psi_{II}(x,y,t) = \frac{1}{\sqrt{2}} \sum_{n=-\infty}^{\infty} \Bigg[& \begin{pmatrix} b_n e^{iq_x^{(n)}x} + c_n e^{-iq_x^{(n)}x} \\ s'_n \left(b_n e^{iq_x^{(n)}x + i\theta_n} - c_n e^{-iq_x^{(n)}x - i\theta_n} \right) \end{pmatrix} \times \\ & \times e^{ik_y y} e^{-in\omega t} \Bigg] \sum_{m=-\infty}^{\infty} \left[J_m \left(\frac{eV}{\hbar\omega} \right) e^{-i(E+m\hbar\omega)t/\hbar} \right], \end{aligned} \tag{3.33}$$

with notations $s'_n = sign(E + n\hbar\omega - eV_0)$, $q_x^{(n)} = \sqrt{\left(\frac{E-eV_0+\hbar\omega n}{\hbar v_f}\right)^2 - k_y^2}$, $\theta_n = \tan^{-1}(k_y/q_x^{(n)}))$. In the most general case, we can have evanescent waves inside region II, then $e^{i\theta_n}$ would be replaced by $\eta'_n = s'_n \frac{q_x^{(n)}+ik_y}{|q_n|}$. The wave in the third region has the form $\Psi_{III} = \Psi_t$. Notice, however, that for all sidebands we still assume specular reflection, thus having y-component of the wavevector conserved.

By matching the wavefunctions at the region boundaries one can get a set of equations for unknown coefficients r_n, t_n, b_n, c_n. This set will contain an infinite number of equations since index n runs over all possible integers. Here we present it in the general form:

$$\begin{cases} \delta_{n,0} + r_n = \sum\limits_l \left[(b_l + c_l) J_{n-l}(\zeta)\right] \\ \delta_{n,0}\eta_n + r_n\bar{\eta}_n = \sum\limits_l s'_l\left[(b_l e^{i\theta_l} - c_l e^{-i\theta_l}) J_{n-l}(\zeta)\right] \\ t_n = \sum\limits_l \left[(b_l e^{iq_l D} + c_l e^{-iq_l D}) J_{n-l}(\zeta)\right] \\ t_n = -\bar{\eta}_n \sum\limits_l s'_l\left[(b_l e^{i\theta_l} e^{iq_l D} - c_l e^{-i\theta_l} e^{-iq_l D}) J_{n-l}(\zeta)\right] \end{cases} \tag{3.34}$$

Here we already used the fact that $\bar{\eta}_n = -1/\eta_n$ by construction. Due to the complicated structure of the set of equations, we have not obtained an exact solution for an infinite number of sidebands. In this work, we present approximated solutions for $|n| < 2$.

Approximated solutions

If now we look at the form of Bessel functions $J_n(\zeta)$, their magnitudes depend strongly on the argument $\zeta = \frac{eV}{\hbar\omega}$. For low values $\zeta \ll 1$, Bessel functions decay rapidly with increasing order n, and one can show that:

$$J_n(\zeta) \approx \left(\frac{n}{|n|}\right)^{|n|} \zeta^{|n|} \frac{2^{-|n|}}{|n|!}, \quad \zeta \ll 1 \tag{3.35}$$

Therefore, the contributions of sidebands can be neglected for higher orders. Already for $\zeta < 0.1$ there is more than one order of magnitude difference between J_0 and J_1, thus virtually all sidebands can be neglected. Physically, it can be easily interpreted: the sideband energy separation $\hbar\omega$ becomes so big comparing to the driving energy eV, that virtually no charge carriers can scatter into states other than the main energy band.

In the general case $\zeta > 1$, we can examine the behavior of the Bessel function in its explicit form:

$$J_n(\zeta) = \frac{1}{\pi} \int\limits_0^\pi \cos(nx + \zeta \sin x) \tag{3.36}$$

With condition $n > \zeta$ we can say $\cos(nx + \zeta \sin x) \approx \cos(nx)$ thus giving $J_n(\zeta) \approx J_n(0) = 0$. So again, the infinite series can be truncated after an arbitrary $n > \zeta$, and a finite set of equations is solvable. From here it is already explicit that for small enough ζ we can truncate already at $n = 1$. Therefore, assuming that our parameter ζ is small enough, we can investigate the linear terms in expansion around the static case, setting $\zeta^2 = 0 \implies J_{|n|>1}(\zeta) = 0$.

Let us write again the original set of equations:

$$\begin{cases} \delta_{n,0} + r_n = \sum\limits_l [(b_l + c_l) J_{n-l}(\zeta)] \\ \delta_{n,0}\eta_n + r_n\bar{\eta}_n = \sum\limits_l s'_l[(b_l e^{i\theta_l} - c_l e^{-i\theta_l}) J_{n-l}(\zeta)] \\ t_n = \sum\limits_l [(b_l e^{iq_l D} + c_l e^{-iq_l D}) J_{n-l}(\zeta)] \\ t_n = -\bar{\eta}_n \sum\limits_l s'_l[(b_l e^{i\theta_l} e^{iq_l D} - c_l e^{-i\theta_l} e^{-iq_l D}) J_{n-l}(\zeta)] \end{cases} \tag{3.37}$$

We can notice that the coupling between them is governed by J_{n-l}, so the terms containing ζ^2 or higher can be neglected in linear approximation. Since the driving term $\delta_{n,0} \neq 0$ exists only for $n = 0$, the equations for $n = 2$ are already coupled through ζ^2, and therefore we can truncate our set of equations just before them, giving $n, l = -1, 0, 1$. Now, this truncated set of 12 linear equations can be easily solved, giving:

$$\begin{aligned} &t_n = n\tfrac{\zeta}{2}\tfrac{\cos\phi_0}{\cos\phi_0\cos\theta_0\cos(q_0D)+i\sin(q_0D)(\sin\theta_0\sin\phi_0-s_0s'_0)}\times \\ &\times\tfrac{-\bar{\eta}_n}{-\bar{\eta}_n\cos\theta_n\cos(q_nD)+i\sin(q_nD)(\sin\theta_n\frac{k_y}{|k^{(n)}|}-s_ns'_n)}\times \\ &\times[i(\eta_0+\eta_n)(s'_n\cos\theta_0\sin q_nD - s'_0\cos\theta_n\sin q_0D)+ \\ &+(\cos\theta_n\cos(q_0D+\theta_0)-\cos\theta_0\cos(q_nD+\theta_n))+ \\ &+\eta_0\eta_n(\cos\theta_n\cos(q_0D-\theta_0)-\cos\theta_0\cos(q_nD-\theta_n))], \quad n=\pm 1 \end{aligned} \tag{3.38}$$

The main band transmission amplitude t_0 remains unchanged comparing to the static case, since the correction to it comes with ζ^2, and we neglected those terms. We have already assumed that we have a plane wave inside the barrier by using angular notation θ, imposing a restriction on the barrier to be high enough. To simplify things even further, let us introduce the high-barrier approximation $E_f \pm \hbar\omega \ll V_0$ so that we can safely put $\theta_n = 0$. With this assumption, (3.38) is reduced to:

$$\begin{aligned} & t_n = t_{s0}\, n\, \tfrac{\zeta}{2} \tfrac{k_x^{(n)} - ik_y}{k_x^{(n)} \cos q_n D - i s_n s_n' \sin q_n D\, |k^{(n)}|} \times \\ & \times [i(\eta_0 + \eta_n)(s_n' \sin q_n D - s_0' \sin q_0 D) + \\ & + (1 + \eta_0 \eta_n)(\cos q_0 D - \cos q_n D)], \quad n = \pm 1 \end{aligned} \tag{3.39}$$

One could compare the procedure used in here, with the one in [28]. The authors of the mentioned paper use analogical approach in the sense of mathing the wavefunctions at the boundaries and looking at $|n| < 2$ case with linear expansion in terms of driving parameter. However, we can find that our result is more general since we use general momentum notation instead of phase or angles. In contrast to them, we can examine evanescent wave solutions behavior, explained in the next chapter.

3.3.3 Transmission eigenvalues

By simple analysis of (3.39) we can see that it contains some interference terms, and is proportional to the value of the driving parameter ζ. Therefore, we can always present the higher-band transmissions on this natural scale, dividing by the driving parameter.

For evanescent waves $k_x^{(n)}$ becomes imaginary. Since such transmission waves should decay at $x \to +\infty$, we set it to have $\mathrm{Im}[k_x^{(n)}] > 0$. The concept is easy to visualize by using Dirac cone crossections for different values of energy. In Fig. 3.9 we examine possible behavior patterns. Dispersion relation $k_x^{(n)\,2} + k_y^2 = E + n\hbar\omega$ projects itself as circles in k_{xy} plane. Whenever the line of k_y conservation does not cross the circle $k_x^{(n)\,2} + k_y^2 = E + n\hbar\omega$ we get evanescent waves. This starts happening after a certain critical angle $\phi_{crit}^{(n)} = \arcsin[\frac{|E+n\hbar\omega|}{|E|}]$, denoted by the green line in Fig. 3.9(b). The other two black lines illustrate the case of plane waves (three circles crossed) and evanescent waves (only two circles crossed). In the shown example, scattering into a hole results in an evanescent wave. Also it is important that the x-projection of the momentum is opposite in magnitude for electrons and holes propagating in the same direction. Therefore, blue and red dots in the figure appear on different sides with respect to k_y axis. If $|E + n\hbar\omega| > |E|$ there is no critical angle, e.g. there is no way to have evanescent waves for such Fermi levels. Due to the symmetry of the dispersion relation the concept of critical angle holds in the same fashion for both, electrons and holes.

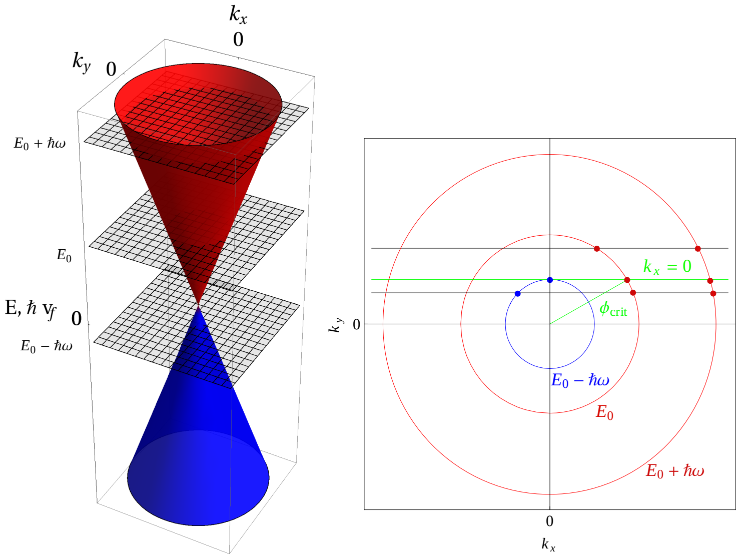

(a) Dispersion relation in k space. Red stands for electron-like behaviour, blue for hole-like

(b) k_{xy} plane projections. Limiting case between plane and evanescent wave solutions is indicated by the green line.

Figure 3.9: Energy band cross sections of the Dirac cone.

With this in mind let us plot the transmission probabilities for different values of Fermi energy and angle of incidence. By examining resulting Fig. 3.10 we can see that transmissions to the higher and lower sidebands are almost mirroring images of each other, so let us concentrate on figure (b) first, responsible for T_{-1}. For energies $E < 0$, the transmission probability behaves normally, resembling the features we have already seen in the static case. Positions of the fringes coincide with those in T_0 signalling, that t_{s0} in (3.39) makes the main contribution there. The critical angle is shown by green lines in the figure. The region not contained between them corresponds to the evanescent waves case. The intersection point of the green curves is at $E = n\hbar\omega$, we have set $\omega = 4v_f/d$ in the presented example.

For $E < 0$ the behavior is always hole-like, in any region of the barrier, and the waves never turn evanescent. However, once we cross $E_F = 0$, the incident wave starts showing electron-like behavior. In the small region $0 < E < \hbar\omega$ it actually scatters into a hole. But due to Dirac cone symmetry, particle type conversion does not affect the transmission pattern, just as in

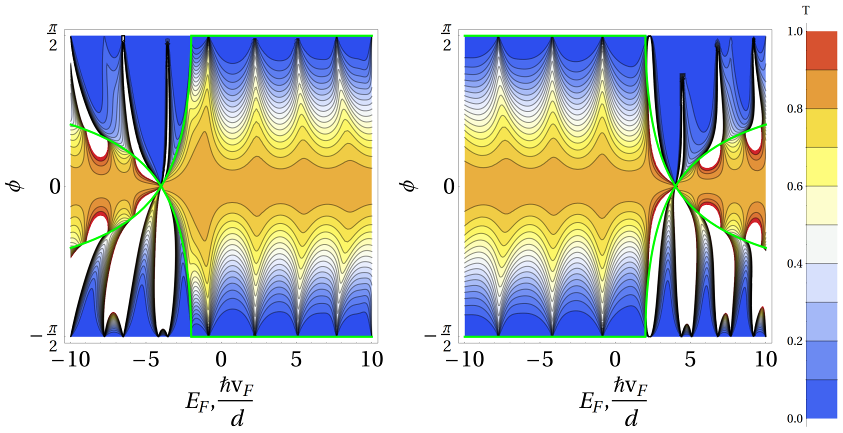

(a) T_1/ζ^2

(b) T_{-1}/ζ^2

Figure 3.10: Transmission probabilities for the sidebands. Critical angle shown by green curves. $\omega = 4v_F/d$

static Klein tunneling case.

Another feature present in Fig. 3.10 are the peaks larger than unity on the scale of ζ^2. In general this is not an issue, since the peaks are allowed to go high up to $1/\zeta^2$. Nevertheless, there is no ζ entering the expressions other than the prefactor we divided out, and the peaks get higher than $1/\zeta^2$ anyway, signalling that something wrong happens, since the transmission probability cannot get over unity unless we are producing some extra particles in the barrier.

By taking a closer look at the analytic formula one can notice that the denominator can be zero at some points. Unlike the original static case, where the denominator contained both, real and imaginary contributions, for the case of evanescent waves it is purely imaginary, and can turn into zero. Let us plot the contribution of prefactor $\left|\frac{k_x^{(n)}-ik_y}{k_x^{(n)}\cos q_nD-is_ns_n'\sin q_nD\,|k^{(n)}|}\right|$ separately. If in Fig. 3.10 we compare the features of the left plot with the prefactor plot on the right, we clearly see that indeed this prefactor is the major contributor to the "unphysical" peaks we are observing. The positions and shapes of the peaks are very similar for the two figures. We can also note, that high peaks in the evanescent region are affecting the picture in the propagating wave region.

Remarkably, these outbrakes are even enhanced when they coincide with

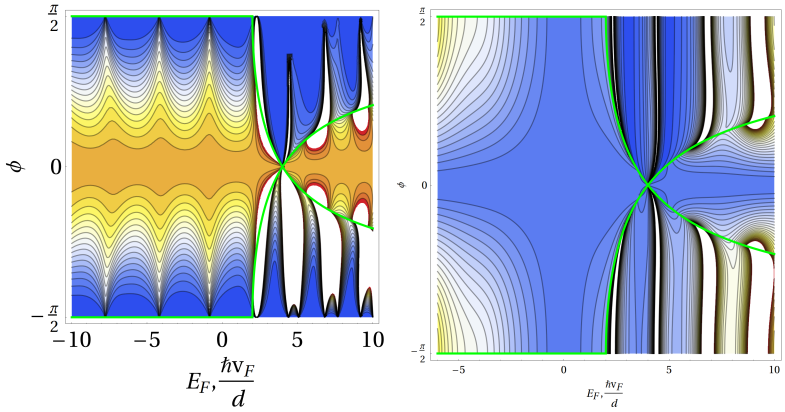

(a) T_{-1}/ζ^2

(b) prefactor

Figure 3.11: Evanescent peaks origin.

the $T_0 = 1$ fringe peaks in the normal region. In addition, the peaks are not symmetric on vertical reflection - they are wider for the negative ϕ then for positive ones, this holds for both, T_{-1} and T_1. This is due to the chirality of the particles in K valley we are examining, they are favouring clockwise path, while in K' valley the situation would be reversed.

Checking the expression for the prefactor in evanescent region, we can see, that the denominator in such case can turn to zero, thus resulting in a pole, and transmission probability diverging. These points are true singularities. So what does exactly happen at those points? We have evanescent waves on either side of the barrier, thus effectively the particle is trapped within the barrier as in a case of quantum well. We have not introduced any finite particle lifetime, assuming their speed is high enough to contribute to current. Therefore, in this case the particle just stays trapped inside the barrier indefinitely. It is a true bound state. This effect tells us that the first-order perturbation theory is breaking down in evanescent regions, inclusion of higher-order terms is needed. A naive guess would be that then the particle would be able to escape from the barrier by transition to other higher-order states, thus just a quasi-bound state would be formed.

However, we still can proceed with the calculation of the conductance in graphene, assuming we are calculating it far away from the barrier, so that the evanescent waves do not contribute to the current. And this is exactly the assumption we already made in the beginning, proposing source, drain and top gate to be far away from each other. In terms of numbers, since evanescent waves decay as $e^{-|k_x|x}$ and $|\hbar v_F k_x| < |E| < eV_0$, in order for our limit to be experimentally possible, we the distance between the contacts should be much larger than $\frac{\hbar v_F}{e\,V_0} \approx \frac{10\,\mathrm{Voltz}}{V_0}$ nm, which is achievable. Now let us continue to the conductance calculation.

3.3.4 AC conductance in graphene

The procedure here is similar to the static case. We follow similar steps to the done in Section 3.2.5 and Appendix A. We start with the expression under the integral of (3.15):

$$\begin{aligned}
&\Psi^{\dagger}_{k,\phi}\sigma_x\Psi_{k,\phi} = \tfrac{1}{2}\sum_{n,m} t_n^* t_m \left(s_n\eta_n^* + s_m\eta_m\right) e^{i(k_x^{(m)}-k_x^{(n)*})(x-D)} e^{i(n-m)\omega t} = \\
&= \tfrac{1}{2}\sum_{n,m} t_n^* t_m s_n \tfrac{k_x^{(n)*}-ik_y}{|k^{(n)}|} e^{i(k_x^{(m)}-k_x^{(n)*})(x-D)} e^{i(n-m)\omega t} + \\
&+ \tfrac{1}{2}\sum_{n,m} t_n^* t_m s_m \tfrac{k_x^{(m)}+ik_y}{|k^{(m)}|} e^{i(k_x^{(m)}-k_x^{(n)*})(x-D)} e^{i(n-m)\omega t} = \\
&= \mathrm{Re}\left[\sum_{n,m} t_n^* t_m \eta_n^* e^{i(k_x^{(m)}-k_x^{(n)*})(x-D)} e^{i(n-m)\omega t}\right]
\end{aligned} \tag{3.40}$$

Here we decomposed the original sum into two separate sums, and by interchanging indices n and m in one of those sums we get precisely the complex conjugate of the other, thus the integrand is always real.

Next, the operator product averages will give us Fermi functions, which under zero-temperature approximation will reduce the integration over energy to the point $E = E_F$. The corresponding conductance would therefore be:

$$G_x = \frac{2e^2}{\pi h}\int_{-\pi/2}^{\pi/2} \mathrm{d}\phi\, \mathrm{Re}[\sum_{n,m} t_n^* t_m \eta_n^* e^{i(k_x^{(m)}-k_x^{(n)*})(x-D)} e^{i(n-m)\omega t}] \tag{3.41}$$

Then we simply can integrate over the allowed region only: $|\phi| < |\phi_{crit}|$, and the evanescent peak outbreaks in the allowed region discussed above should not drastically change the final picture.

Thus, we assume $k_x^{(n)} \in \Re$. Since the transmission amplitude is proportional to ζ, coming back to the conductance calculation 3.41, we are limited

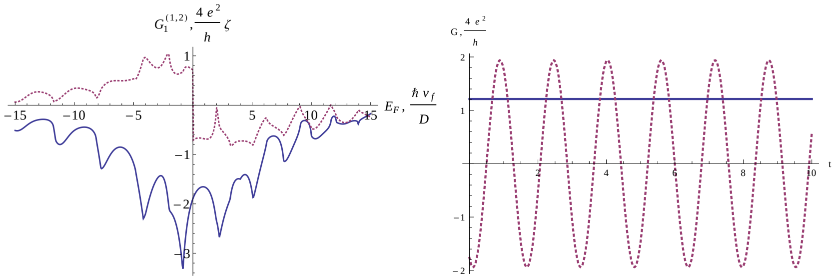

(a) Energy dependence of dynamic conductance components. $G_1^{(1)}$ is solid, $G_1^{(2)}$ is dotted

(b) Static (solid) and dynamic (dotted) conductance components at $E_F = 5\hbar v_f/d$. Latter scaled by $1/\zeta$

Figure 3.12: Dynamic conductance energy and time dependence.

to $n, m = -1, 0, 1$:

$$G_x(E_F, x, t) = \frac{2e^2}{\pi h}\sum_{n,m=-1}^{1} \mathrm{Re}\Big[\int_{-\phi_{crit}^{(nm)}}^{\phi_{crit}^{(nm)}} \mathrm{d}\phi\, t_n^* t_m s_n e^{-i\phi_n} e^{i(k_x^{(m)}-k_x^{(n)})(x-D)} e^{i(n-m)\omega t}\Big] \tag{3.42}$$

Here we must note that the critical angle for the integration is determined by the minimal critical angle of the two interfering energy bands: $\phi_{crit}^{(nm)} = \mathrm{Min}[\phi_{crit}^{(n)}, \phi_{crit}^{(m)}]$. We can see, that now conductance aquired space and time dependence unlike the static case. Both dependences are conneted to the driving frequency. Examining $n = m = 0$ case one can uncover the static part of the conductance, which remains unchanged comparing to the original case. Other contributions to it, resulting from $n = m \neq 0$ are of higher orders in ζ, so we neglect them.

Let us at first look at the energy and time dependence, by choosing a particular position x such that $e^{i(k_x^{(1)}-k_x^{(0)})(x-D)} = 1$. This will ensure no position phase factors to come along with sideband contributions. Then we can proceed to the conductance calculation. To analyse the time-dependent terms we introduce the following notation: $G_x = G_0 + G_1^{(1)}\cos\omega t + G_1^{(2)}\sin\omega t$. We already know how G_0 looks like, so let us plot $G_1^{(1,2)}$.

From 3.12(a) we can see that there are large peaks in the dynamic conductance components in the region of particle type conversion. After the point $|E_F| = \hbar\omega \quad$ (ω taken $4v_f/d$), the oscillation amplitudes becomes small. For (b) we plotted static and dynamic parts of the conductance, latter scaled by the factor of $1/\zeta^2$, so in reality it is much smaller since $\zeta \ll 1$.

3.3.5 Adiabatic driving

So far, we have examined the system in high V_0 and small ζ regime. In the previous section we displayed some results beyond analytical model presented in here. Let us continue investigation of the system in various limits.

We know, that the driving parameter $\zeta = \frac{eV}{\hbar\omega}$ depends on two variables. In an experimental setup, both, driving voltage and frequency can vary on a large scale. In our first-order expansion in low ζ we have only two sidebands. We know, that energies for the sidebands are $E_{\pm 1} = E \pm \hbar\omega$. If natural scale for energy in graphene barrier problem is $\frac{\hbar v_F}{D}$ then the corrections from sidebands would play a role only if they are comparable with this scale.

Now, having an expression for conductance as a function of driving frequency ω, we can actually expand it for small frequencies. The conditions for that are already set:

$$\hbar\omega \ll \frac{\hbar v_F}{D} \implies \omega \ll \frac{v_F}{D} \tag{3.43}$$

Then, under these circumstances, what physically happens is that the charge carriers fly through the barrier faster than needed to be affected by the AC part of the barrier - they do not "feel" it. Indeed, the naive assumption about the natural scale, or the scale on which the scattering amplitudes change significantly, results in a frequency limit depending only on Fermi velocity of charge carriers and barrier width. Now, working on a nanoscale we can consider an example of $D = 100$ nm. Then, the adiabatic behavior of the system hold to frequencies of 3×10^{13} Hz $= 30$ THz, which is well beyond the limit of modern electronics. Having thinner barriers in the downscaling race would result even in higher adiabatic limit. The results presented in previous sections corresponded to $\omega = 4\frac{v_F}{D}$, thus we examined the crossover regime between the region with effective zero contribution from sidebands, and strong driving.

Now, if we consider strong driving regime, we will get multiple sidebands, but it does not change the natural energy scale. So, for n sidebands we will get the adiabatic limit:

$$n\omega \ll \frac{v_F}{D} \tag{3.44}$$

But we already know, that the number of sidebands is effectively governed

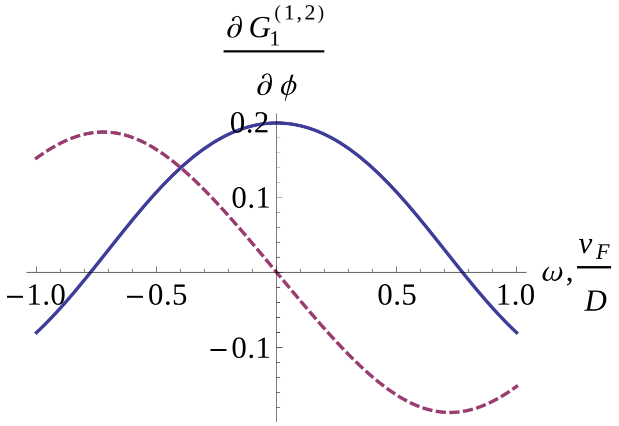

Figure 3.13: $\frac{\partial G_1^{(1)}}{\partial\phi}$(solid) and $\frac{\partial G_1^{(2)}}{\partial\phi}$(dashed) as functions of frequency. $E = 10\frac{\hbar v_F}{D}$, $\phi = \frac{\pi}{4}$. Vertical axis has arbitrary scale

by $n \approx \mathrm{Int}[\zeta]$. Thus, adiabatic restriction would lead us to:

$$n\omega \ll \frac{v_F}{D} \implies \zeta\omega \ll \frac{v_F}{D} \implies \frac{eV}{\hbar} \ll \frac{v_F}{D} \implies V \ll \frac{\hbar v_F}{eD} \tag{3.45}$$

Again, it is a very intuitive result. Here we can see that the strength of driving should not exceed the natural unit of the energy scale. Now, having the same barrier of 100 nm we would get the limit on strength of driving around 20 mV, which is in accessible range. Therefore, we can actually tune the transistor in or out the adiabatic regime.

Non-adiabatic regime is generally connected with increased power losses and noise in the sytem, so let us concentrate on the first-order approximation around pseudo-static case. We will expand the conductance to the first order in ω in n=1 approximation.

As a check, one can do an expansion of (3.42) to the 0th order first. It is relatively easy, because $t_{\pm 1} = 0$ in this case, thus only t_0, correspondning to the static tunnenling, contributes to the conductance.

For the first-order expansion we decompose it into the form $G_x = G_0 + G_1^{(1)}\cos\omega t + G_1^{(2)}\sin\omega t$ from (3.42). It is easy to see, that:

$$\begin{aligned} G_1^{(1)} &= \tfrac{2e^2}{\pi h}\int \mathrm{d}\phi\, \mathrm{Re}[t_0^*(t_1 + t_{-1})]; \\ G_1^{(2)} &= -\tfrac{2e^2}{\pi h}\int \mathrm{d}\phi\, \mathrm{Im}[t_0^*(t_1 - t_{-1})] \end{aligned} \tag{3.46}$$

Now the integration over angles ϕ does not affect the dependence of the conductance components on frequency, thus we will concentrate on the expressions under the integrals instead. The expansion of tunneling amplitudes in terms of frequency can be quite lengthy and will not be included here. However, to illustrate author's point of view we present Fig. 3.13 showing the conductance components at arbitrary energy and angle as functions of frequency in the region of propagating waves. From this figure, we can clearly see, that the "in-phase" component $G_1^{(1)}$ is a constant plus a quadratic in frequency term for small $\omega \ll 1$, while the "out-of-phase" $G_1^{(2)}$ is linear. Therefore, since we are expanding to the first order in omega, the lowest order $G_1^{(1)}$ has is 0th - it has no frequency dependence in 1st-order approximation. This, in turn, leads us to the fact that for sufficiently small ω we are left with in-phase component only - it remains constant but non-zero for low frequencies, while $G_1^{(2)}$ approaches zero. It lies in line with the concept of adiabatic driving. When the frequency is low enough, the charge carriers taking part in transport pass through the barrier fast enough to consider it static. The height of static barrier changes as $\cos \omega t$, as we assumed, thus only $G_1^{(1)}$ is preserved. With increasing frequency to levels when the electrons start to be affected directly by it, the nonlinear effects start to take place and out-of-phase component increases in magnitude. For larger driving parameter we expect higher harmonics to appear in the expression for conductance, resulting from $n\omega$ sidebands.

Another observation we can draw from Fig. 3.13 is that the out-of-phase component is always negative for positive driving frequencies. Therefore, it always decreases the overall conductance, signaling us that the nonlinear effects are to be avoided in case we need high conductance in the sample. And generally we want high conductance, since it increases the amplitude of the current signal, which is the key point in differentiating it from the background noise in devices. From Fig. 3.13 we can observe that $G_1^{(1)}$ and $G_1^{(2)}$ can be on the same order of magnitude in general, thus the contribution from the nonlinear effects can be not negligible but rather a major term.

A related conclusion we can derive is that the out-of-phase component is responsible for electrons interacting with the oscillating barrier, we understand that it results from sideband effects, therefore energy quanta are transferred during the scattering between different sidebands. This results in power being dissipated in the device, and again, we want to avoid this process to get less energy used by it. In addition, unwanted heating of a small device can result in its malfunction or even destruction, therefore we want to minimize this effect.

Chapter 4

Static noise in graphene

Noise plays an important role in many electronic applications. Usually we want to get rid of it, since it distorts the original signals we try to pass through a particular device.

In this chapter we calculate current-current correlations for the static barrier in graphene using the operator framework developed in Chapter 3. More on this matter can be found in [29].

Section 4.1 will contain the derivation of general formula, Sec. 4.2 will concentrate on zero-frequency noise, giving a general formula for it, and discussing the behavior along with comparison to results of other groups.

4.1 General formula

4.1.1 Operator formalism

We define the time-dependent noise power as the self-correlation function of current:

$$S_x(t,\tau) = \left\langle \hat{I}_x(t)\hat{I}_x(t+\tau) \right\rangle - \left\langle \hat{I}_x(t) \right\rangle \left\langle \hat{I}_x(t+\tau) \right\rangle \tag{4.1}$$

The second term is the mean of the signal, we subtract it in order to get rid of the signal mean, which is contained in the first term. In this representation we see that the electrons may be injected at different times t from the leads.

In previous sections, we saw that the static current possesses no time dependence due to the cancellation of injection times in operator averages.

However, such cancellation might not work for the noise calculation:

$$\begin{aligned}&\left\langle \hat{I}(t_1)\hat{I}(t_2)\right\rangle = \sum_{\alpha,\alpha',\alpha'',\alpha'''} \left\langle \tfrac{e^2 v_f^2}{(2\pi)^8} \int \Big[\mathrm{d}k\mathrm{d}\phi\mathrm{d}k'\mathrm{d}\phi'\mathrm{d}k''\mathrm{d}\phi''\mathrm{d}k'''\mathrm{d}\phi''' \hat{a}^{\dagger}_{\alpha}(k,\phi,t_1)\times \right.\\ &\left.\times a_{\alpha'}(k',\phi',t_1) a^{\dagger}_{\alpha''}(k'',\phi'',t_2) a_{\alpha'''}(k''',\phi''',t_2) \Psi^{\dagger}_{\alpha}\sigma_x \Psi'_{\alpha'} \Psi''^{\dagger}_{\alpha''}\sigma_x \Psi'''_{\alpha'''}\Big] \right\rangle\end{aligned} \tag{4.2}$$

Now we have to deal with the average product of four operators: $\left\langle \hat{a}^{\dagger}_{\alpha}(k,\phi,t_1) a_{\alpha'}(k',\phi',t_1) a^{\dagger}_{\alpha''}(k'',\phi'',t_2) a_{\alpha'''}(k''',\phi''',t_2)\right\rangle$, which is non-zero only if we have repeating indices for creation and annihilation operators, so that they are paired up. Therefore, it can be decomposed into these possible combinations:

$$\begin{aligned}&\left\langle \hat{a}^{\dagger}(t_1)\hat{a}'(t_1)\hat{a}''(t_2)^{\dagger}\hat{a}'''(t_2)\right\rangle = \left\langle \hat{a}^{\dagger}(t_1)\hat{a}(t_1)\hat{a}''^{\dagger}(t_2)\hat{a}''(t_2)\right\rangle + \\ &+ \left\langle \hat{a}^{\dagger}(t_1)\hat{a}''(t_1)\hat{a}''^{\dagger}(t_2)\hat{a}(t_2)\right\rangle\end{aligned} \tag{4.3}$$

Here primes denote the indices α, k, ϕ for a short notation. Kronecker delta functions are also ommitted for the next two steps. Now we can see that after pairing we can split the four-operator into two-operator averages, since operators with different primes do not act on each other. Therefore:

$$\begin{aligned}&\left\langle \hat{a}^{\dagger}(t_1)\hat{a}'(t_1)\hat{a}''^{\dagger}(t_2)\hat{a}'''(t_2)\right\rangle = \left\langle \hat{a}^{\dagger}(t_1)\hat{a}(t_1)\right\rangle \left\langle \hat{a}''^{\dagger}(t_2)\hat{a}''(t_2)\right\rangle + \\ &+ \left\langle \hat{a}^{\dagger}(t_1)\hat{a}(t_2)\right\rangle \left\langle \hat{a}''(t_1)a''^{\dagger}(t_2)\right\rangle\end{aligned} \tag{4.4}$$

Now the first biproduct will eventually cancel with the mean of the signal, which we subtracted explicitly. Since we already know how to compute averages of two operators, we can apply it directly in here, leading to:

$$\begin{aligned}&S_x(\tau) = \tfrac{e^2 v_f^2}{(2\pi)^4} \sum_{\alpha,\alpha''} \int \mathrm{d}k\mathrm{d}\phi\mathrm{d}k''\mathrm{d}\phi'' \Big[f_{\alpha}(\hbar v_f k)\left(1 - f_{\alpha''}(\hbar v_f k'')\right)\times \\ &\times e^{i v_f (k-k'')\tau} |\Psi^{\dagger}_{\alpha}(k,\phi)\sigma_x \Psi_{\alpha''}(k'',\phi'')|^2 \delta_{k_y k''_y}\Big]\end{aligned} \tag{4.5}$$

Detailed derivation of the formula above is found in Appendix B.

4.1.2 Frequency domain

At this point let's work over two scenarios separately: $\alpha = \alpha''$ and $\alpha \neq \alpha''$. Consider the first one:

$$\begin{aligned}&S_x^{\alpha=\alpha''}(\tau) = \tfrac{e^2 v_f^2}{(2\pi)^4} \sum_{\alpha} \int \mathrm{d}k\mathrm{d}\phi\mathrm{d}k''\mathrm{d}\phi'' \Big[f_{\alpha}(E)\left(1 - f_{\alpha}(E'')\right)\times \\ &\times e^{i v_f (k-k'')\tau} |\Psi^{\dagger}_{\alpha}(k,\phi)\sigma_x \Psi_{\alpha}(k'',\phi'')|^2 \delta_{k_y k''_y}\Big]\end{aligned} \tag{4.6}$$

Let us now switch to the frequency domain by taking a Fourier transform:

$$S_x(\Omega) = \int \mathrm{d}\tau S_x(\tau) e^{-i\Omega\tau} \tag{4.7}$$

The sinusoids in time domain will transform into delta functions in frequency: $\int \mathrm{d}\tau e^{\pm i(E-E'')\tau/\hbar - i\Omega\tau} = 2\pi\delta\Big(\pm\frac{E-E''}{\hbar} - \Omega\Big) = h\delta(\pm(E-E'') - \hbar\Omega)$, therefore:

$$\begin{aligned} S_x^{\alpha=\alpha''}(\Omega) = \tfrac{e^2}{h(2\pi)^2} \sum_\alpha \int & \mathrm{d}E\mathrm{d}\phi\mathrm{d}\phi''\delta_{k_y k_y''}\Big[f_\alpha(E)\left(1-f_\alpha(E-\hbar\Omega)\right)\times \\ & \times|\Psi_\alpha^\dagger(E,\phi)\sigma_x\Psi_\alpha(E-\hbar\Omega,\phi'')|^2 + f_\alpha(E)\left(1-f_\alpha(E+\hbar\Omega)\right)\times \\ & \times|\Psi_\alpha^\dagger(E,\phi)\sigma_x\Psi_\alpha(E+\hbar\Omega,\phi'')|^2\Big] \end{aligned} \tag{4.8}$$

Now consider the case when $\alpha \neq \alpha''$. Let us expand over the two cases of reservoirs available, left and right:

$$\begin{aligned} S_x^{\alpha\neq\alpha''}(\tau) = \tfrac{e^2 v_f^2}{(2\pi)^4} \int & \mathrm{d}k\mathrm{d}\phi\mathrm{d}k''\mathrm{d}\phi''\delta_{k_y k_y''}\Big[f_L(E)\left(1-f_R(E'')\right)\times \\ & \times e^{i(E-E'')\tau/\hbar}|\Psi_L^\dagger(k,\phi)\sigma_x\Psi_R(k'',\phi'')|^2 + f_R(E)\left(1-f_L(E'')\right)\times \\ & \times e^{i(E-E'')\tau/\hbar}|\Psi_R^\dagger(k,\phi)\sigma_x\Psi_L(k'',\phi'')|^2\Big] \end{aligned} \tag{4.9}$$

Notice that two Ψ parts in the integrand are indentical if we switch k with k'' and ϕ with ϕ'' in one of them, so we split the integral into two, flip the variables in one of them, and recombine everything back, leading to:

$$\begin{aligned} S_x^{\alpha\neq\alpha''}(\tau) = \tfrac{e^2}{(2\pi)^2 h^2} \int & \mathrm{dEd}\phi\mathrm{dE}''\mathrm{d}\phi''\delta_{k_y k_y''}\Big[|\Psi_L^\dagger(E,\phi)\sigma_x\Psi_R(E'',\phi'')|^2\times \\ & \times\left[f_L(E)\left(1-f_R(E'')\right)e^{i(E-E'')\tau/\hbar} + f_R(E'')\left(1-f_L(E)\right)e^{i(E''-E)\tau/\hbar}\right]\Big] \end{aligned} \tag{4.10}$$

Let us now switch to the frequency domain:

$$\begin{aligned} S_x^{\alpha\neq\alpha''}(\Omega) = \tfrac{e^2}{(2\pi)^2 h}\int & \mathrm{dEd}\phi\mathrm{d}\phi''\Big[\Big|\Psi_L^\dagger(E,\phi)\sigma_x\Psi_R(E-\hbar\Omega,\phi'')\Big|^2\times \\ & \times f_L(E)(1-f_R(E-\hbar\Omega)) + \Big|\Psi_L^\dagger(E,\phi)\sigma_x\Psi_R(E+\hbar\Omega,\phi'')\Big|^2\times \\ & \times f_R(E+\hbar\Omega)\left(1-f_L(E)\right)\Big]\delta_{k_y k_y''} \end{aligned} \tag{4.11}$$

Finally, if we combine (4.8) and (4.11) we get the full formula for noise: $S_x(\Omega) = S_x^{\alpha\neq\alpha''}(\Omega) + S_x^{\alpha=\alpha''}(\Omega)$. Now, integration over several different parameters may be done numerically, but we cannot see from it the general behavior of the system. Therefore, let us concentrate on a particular limit.

4.2 Zero-frequency noise

4.2.1 Derivation

We now examine the zero-frequency case in detail. Assuming $\Omega = 0$ we get two different energy points $E \pm \hbar\Omega$ merging into one, simplifying (4.11) to:

$$\begin{aligned} &S_x^{\alpha\neq\alpha''}(0) = \tfrac{e^2}{(2\pi)^2 h}\int \mathrm{dEd}\phi\mathrm{d}\phi''\Big|\Psi_L^\dagger(E,\phi)\sigma_x\Psi_R(E,\phi'')\Big|^2\delta_{k_y k_y''}\times \\ &\times\Big[f_L(E)\left(1-f_R(E)\right)+f_R(E)\left(1-f_L(E)\right)\Big] \end{aligned} \tag{4.12}$$

Let us first focus on the Fermi function contribution to the integrand:

$$\begin{aligned} &f_L(E)\left(1-f_R(E)\right)+f_R(E)\left(1-f_L(E)\right) = \\ &= \tfrac{e^{(E-\mu_L)/k_B\Theta}+e^{(E-\mu_R)/k_B\Theta}}{(1+e^{(E-\mu_L)/k_B\Theta})(1+e^{(E-\mu_R)/k_B\Theta})} \end{aligned} \tag{4.13}$$

Now if we compare it to the difference between two Fermi functions:

$$f_L(E) - f_R(E) = \tfrac{e^{(E-\mu_R)/k_B\Theta}-e^{(E-\mu_L)/k_B\Theta}}{(1+e^{(E-\mu_L)/k_B\Theta})(1+e^{(E-\mu_R)/k_B\Theta})}, \tag{4.14}$$

we notice that the only difference is in nominators. But under zero-temperature approximation they become the same, thus giving us $f_L(1-f_R)+f_R(1-f_L) = f_L - f_R$. Therefore, now we can use the power of the method developed in Appendix A, where we encountered $f_L - f_R$, and reduce the integral to the following:

$$\begin{aligned} &S_x^{\alpha\neq\alpha''}(0) = \tfrac{e^2}{(2\pi)^2 h}\int \mathrm{dEd}\phi\mathrm{d}\phi'' eV\delta(E-E_F)\delta_{k_y k_y''}\Big|\Psi_L^\dagger(E,\phi)\sigma_x\Psi_R(E,\phi'')\Big|^2 = \\ &= \tfrac{e^3 V}{2\pi h}\int \mathrm{d}\phi\Big|\Psi_L^\dagger(E_F,\phi)\sigma_x\Psi_R(E_F,\pi-\phi)\Big|^2 \end{aligned} \tag{4.15}$$

Note that here due to the delta functions $E \to E_F$ and $k_y'' = E_F\sin\phi'' \to k_y = E_F\sin\phi''$, which implies $\sin\phi'' \to \sin\phi$. Finally, at this point we want to compute the mixed product between the wavefunctions. One has to note, that since $\Psi_L(E_F,\phi)$ comes from the left reservoir, ϕ is limited to the region $[-\frac{\pi}{2},\frac{\pi}{2}]$, while $\phi'' \in [\frac{\pi}{2},\frac{3\pi}{2}]$. Therefore, $\sin\phi'' \to \sin\phi \implies \phi'' \to \pi-\phi$ Assume we are measuring the noise in the right part of the reservoir, then Ψ_L would be in the form of a transmitted wave, while Ψ_R of incident onto plus reflected from the barrier. The forms of them can be retrieved from

(3.32) by taking n=0. Simple math shows it to be:

$$\begin{aligned}
&|\Psi_L^{\dagger}(E_F,\phi)\sigma_x\Psi_R(E_F,\pi-\phi)\Big|^2 = \\
&= \tfrac{1}{4}\left|t^{*}e^{-ik_x x}\begin{pmatrix} 1 & se^{-i\phi}\end{pmatrix}\begin{pmatrix} s(e^{ik_x x}e^{i(\pi-\phi)} - re^{-ik_x x}e^{-i(\pi-\phi)}) \\ e^{ik_x x} + re^{-ik_x x}\end{pmatrix}\right|^2 = \\
&= T(E_F,\phi)R(E_F,\phi)\cos^2\phi = T(E_F,\phi)(1-T(E_F,\phi))\cos^2\phi
\end{aligned} \tag{4.16}$$

By plugging this result back into previous equation we get:

$$S_x^{\alpha\neq\alpha''}(0) = \tfrac{e^3V}{2\pi h}\int \mathrm{d}\phi\; T(E_F,\phi)(1-T(E_F,\phi))\cos^2\phi \tag{4.17}$$

Equation (4.8) at zero frequency becomes:

$$\begin{aligned}
&S_x^{\alpha=\alpha''}(0) = \tfrac{e^2}{(2\pi)^2h}\sum_{\alpha}\int \mathrm{d}E\mathrm{d}\phi\mathrm{d}\phi''\delta_{k_yk_y''}\Big[f_\alpha(E)\left(1-f_\alpha(E)\right)\times \\
&\times|\Psi_\alpha^{\dagger}(E,\phi)\sigma_x\Psi_\alpha(E,\phi'')|^2\Big]
\end{aligned} \tag{4.18}$$

Now here the wavefunctions come from the same reservoirs which implies $\delta(k_y-k_y'')=1 \implies \phi=\phi''$. Therefore we get:

$$\begin{aligned}
&S_x^{\alpha=\alpha''}(0) = \tfrac{e^2}{2\pi h}\sum_{\alpha}\int \mathrm{d}E\mathrm{d}\phi\Big[f_\alpha(E)\left(1-f_\alpha(E)\right)\times \\
&\times|\Psi_\alpha^{\dagger}(E,\phi)\sigma_x\Psi_\alpha(E,\phi)|^2\Big]
\end{aligned} \tag{4.19}$$

It is easy to see that under low-voltage and zero-temperature approximations this product turns into zero, so there is no contribution from identical reservoirs to the overall noise.
The total zero-frequency noise is therefore found to be:

$$S_x(0) = \tfrac{2e^3V}{\pi h}\int\limits_{\phi=-\pi/2}^{\pi/2} \mathrm{d}\phi T(E_F,\phi)(1-T(E_F,\phi))\cos^2\phi \tag{4.20}$$

Here we multiplied by a factor of 4 coming due to spin and valley degeneracy.

4.2.2 Results and discussion

If we now plot the formula and compare it to the static conductance we will notice an anti-correlation between these two. Here by anti-correlation we mean that important features of one plot are reversed in the other. Specifically, the minima and maxima are exchanged. This can be readily explained

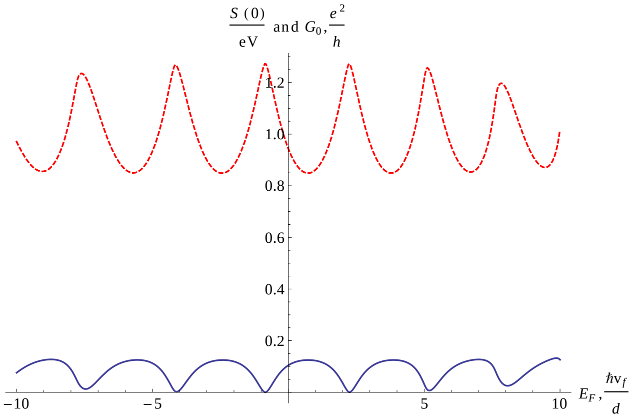

Figure 4.1: Static zero-frequency noise (solid) and conductance (dashed)

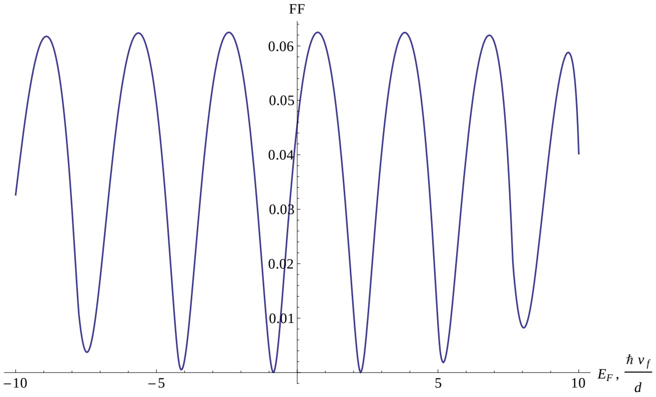

Figure 4.2: Fano factor

by the following argumentation. When the conductance reaches its maximum, the transmission probability is unity, thus there is no reflection and no interference between transferred particles. The only contribution from different reservoirs (4.20) has $1 - T$ factor there, which turns to zero for ideal ballistic conduction. But this holds only in zero-temperature approximation, because for finite temperatures, the noise contribution from the incident wave (identical reservoirs) (4.19) is no longer zero.

We can also compute Fano factor, which resembles an inverse of signal-to-noise ratio:

$$FF = \frac{S_x(0)}{2eI_x} \tag{4.21}$$

The denominator here represents the noise limit for a tunnel-like barrier $T \ll 1$, first derived by Schottky. Low tunneling probability means that the time intervals between individual electrons are infinitely large comparing to the travelling time, in addition, they are random. Thus, the arrivals are uncorrelated and are governed by Poissonian statistics, resulting in the noise being proportional to the current. The Fano factor is plotted in Fig. 4.2.

If checking the obtained values and trying to compare them with those found in the literature, we can take an example of calculation [33], which was verified through experimental observation [34]. In the setup used by these groups, they work on a graphene sheet contained between two electrodes, and the back gate is used in order to shift the Fermi level with respect to the Dirac point. Thus, they do not have scattering barrier in graphene sheet. They concentrate on the limit of $W/L \to \infty$ by reducing L, the distance between electrodes, to zero, while the width is also kept finite, thus giving quantization in the transverse direction, resulting in a discrete number of conduction channels formed between the source and the drain. The electrical transport is realised via evanescent waves coming from reservoirs, something that we do not have in our setup. In this case, the conductance manifests itself as a conductance quantum divided by π, while Fano factor goes to 1/3. From the calculation provided in this work, it is clearly seen that the Fano factor, as well as the conductance, depend on the device geometry. They are defined by the fundamental scattering problem layout. In our case, the current is carried by propagating waves, thus Klein nature of tunneling through the potential barrier plays a major role in the transmission eigenvalues. High transmission peak of order unity for zero-incidence waves lowers the Fano factor, while it is not observed for the layout of groups [33, 34] due to evanescent waves conduction.

Chapter 5

Conclusions and outlook

5.1 Thesis results

The work presented in this thesis partially fulfills the original goals. During the research progress, we encountered bound state formation phenomenon not foreseen from the beginning, thus turning the work to a slightly different direction.

In the scope of the work, we analysed electronic transport through a transistor based on ballistic graphene. We have shown how different transport regimes can be achieved via controlling four available terminals: source, drain, top gate, and back gate. In the setup of large distance between source, drain and gates, we investigated the scattering process from a potential barrier in graphene with both, static and time-dependent behavior.

For the static drive we solved the scattering problem in graphene and 2DEG in specular reflection regime, found the results in agreement with previous studies, and compared two distinct tunneling behaviors. We have followed Landauer approach to electronic current transport and arrived at the corresponding conductances for graphene and 2DEG. Although both types of materials showed generic relations between conductance and barrier tunneling probability, based on scattering problem solutions, we pointed out the important differences between graphene and 2DEG: while the latter shows exponential dependence on energy versus height of the barrier due to normal tunneling, graphene displays Klein tunnneling behavior resulting in weak relation to the barrier height, oscillatory dependence on energy appoaching the conductance quantum for larger energies. Therefore, using graphene in a voltage amplifier or similar structures would not be preferrable due to small conductance variation.

We showed how periodically-driven potential barrier can result in energy sideband formation. In the scattering approach, due to the complicated form of boundary matching conditions between wavefunctions, we had to restrict our solutions to weak AC driving resulting in the analytical results describing $n = \pm 1$ sidebands only. We found our expressions to be in good correspondence with the previous research conducted. However, we deduced that for some angles of incidence, the waves corresponding to sidebands turn evanescent in the region outside of the barrier, thus trapping the propagating waves inside the barrier resulting in a bound state formation. The corresponding transmission eigenvalues showed divergences in the first-order perturbation theory for evanescent solutions. The problem could be tackled by introducing a higher-order perturbation calculation, which resolve them as quasi-bound states eventually leaking out from the barrier. Formation of quasi-bound states is a well-known physical phenomenon in connection to, for instance, the scattering from impurity potentials, also the same effects can be observed in 2DEG systems [35]. The behavior of transmission peaks is known as Fano resonances [30]. The conductance calculation, however, were not affected by this fact, since the source and drain electrodes are positioned sufficiently far away from the top gate in the middle, thus the evanescent solutions will not leak out to the electrodes.

We also showed that the shot noise is greatly reduced in the investigated setup of graphene-based transistor due to Klein tunneling which can result in a better signal-to-noise ratio in real devices. Comparing to the other groups, working in a different regime, the result also manifests how different types of geometry of the device can affect its transport characteristics, while relations between the measured quantities like conductance or shot noise and transmission eigenvalues bear generic nature.

In connection with possible application to real devices, we investigated the adiabatic limit for conductance in graphene, and found that it is easily achievable experimentally, moreover, non-adiabatic limit is almost beyond the reach of today's technology, unless the gate length is held large enough.

5.2 Further research

As the goals were only partially fullfilled, and calculations themselves contained a lot of approximations, the author sees a big room for improvement.

During the final phase of research we found that real devices with the proposed setup should most probably operate in the adiabatic limit, with gate potential considered as static. The potential frequency limit for such applications is in THz frequency range. We found the corresponding fundamental constrictions on our driving parameters. However, due to the lack of time, we were unable to investigate the case completely. Introducing this limit may lead to significant simplifications in the scattering problem, thus further research in this direction may lead to development of analytical expressions for multiple sidebands. Arbitrary driving parameter ζ may be considered unlike first-order approximation used in this work.

When solving the scattering problem, the author has considered only high static barrier limit, for which Klein nature of tunneling in graphene strongly manifests itself. As one of the possible extensions of the theory, we could analyse the opposite limit - zero DC driving potential. Positioning of the Fermi level exactly at the Dirac point enables us to use the symmetry of the Dirac cone, thus resulting in new kinds of ambipolar electronic devices, like frequency multipliers [18]. The general scattering problem presented here can be modified in order to treat this setup and be verified by already existing experimental evidence.

Another area of advance for this research is examination of quasi-bound state formation. Development of a framework to deal with these solutions may lead to some discoveries in relation with Dirac cone symmetry, since unlike 2DEG, the bound states here are not governed by the height of the static potential barrier, but rather by the strength of AC driving. Investigation of Fano resonances with inclusion of multiple side bands on a fundamental level is needed. Yet another interesting point would arise from taking a limit of vanishing width of the barrier, thus approaching delta-potential shape, and comparing the obtained results with the existing calculations for delta-barrier setups [36].

In the parts of the thesis following Landauer-Büttiker theory we did certain approximation, like low potential difference between source and drain, and assumption of zero temperature. Naturally, we can improve the theory by accounting for non-vanishing temperature, examining the effects of thermal excitations on conductance, and especially noise. Also we can look for the energies not only around Fermi point, and see how it affects the transport. These effects are especially interesting when Fermi level is placed exactly at Dirac points. In the absence of cross-sample potential we may still expect non-zero currents flowing into the source/drain electrodes.

For the section describing the noise, we still have not investigated the non-zero frequency case in static driving, and no calculation was performed for AC driven graphene. This is mostly due to the fact described above - in the most probable, adiabatic, case the barrier can be considered as static, thus inclusion of sidebands would not introduce significant effect.

Graphene is still a relatively novel material in the hands of mankind, and it is difficult to estimate its future range of applications, many new effects can still be hidden from the eyes of researchers. Advances in this fascinating area of study can enable whole new types of devices developed for RF communication systems and electronics in general.

Bibliography

[1] H. W. Kroto *et al.*, Nature 318: 162163 (1985)

[2] S. Iijima, Nature 354: 5658 (1991)

[3] K. S. Novoselov *et al.*, Science 306 (5696): 666 (2004)

[4] Y.-M. Lin *et al.*, Science 327: 662 (2010)

[5] L. Liao *et al.*, Nature 467: 305 (2010)

[6] F. Schwierz, Nature Nanotechnology 5: 487 (2010)

[7] P.R. Wallace, Phys. Rev. 71: 622 (1947)

[8] Mouras, S. et al. (1987). "Synthesis of first stage graphite intercalation compounds with fluorides". Revue de Chimie Minerale 24: 572

[9] N. D. Mermin and H. Wagner, Phys. Rev. Lett. 17: 1133 (1966)

[10] L. D. Landau and E. M. Lifshiftz, "Statistical Physics, Part I", Pergamon, Oxford (1980)

[11] L. Meyer *et al.*, Nature 446 (7131): 6063 (2007)

[12] P. Sutter, Nature Materials 8 (3): 17. (2009)

[13] X. Liet al, Science 324 (5932): 1312 (2009)

[14] S.V. Morozov *et al.*, Phys. Rev. Lett 100: 016602 (2008)

[15] R.R. Nair *et al.*, Science 320 (5881): 1308 (2008)

[16] A. Tzalenchuk *et al.*, Nature Nanotechnology 5, 186 - 189 (2010)

[17] V.P. Gusynin and S.G. Sharapov, Phys. Rev. Lett. 95: 146801 (2005)

[18] T. Palacios *et al.*,Communications Magazine, IEEE 48 (6): 122-128 (2010)

[19] M. O. Goerbig, arXiv:0909.1998v2

[20] H. Kroemer, "Quantum Mechanics for Engineering, Material Science, and Applied Physics", Prentice Hall, New Jersey (1994)

[21] M.I. Katsnelson, K.S. Novoselov, and A.K. Geim, Nature Physics: 620-625 (2006)

[22] Y. Nazarov and Y. Blanter, Ch. 1.3.4, ISBN-13 978-0-511-54024-0, Cambridge University Press, New York (2009)

[23] Reich S. *et al.*, Phys. Rev. B 66, 035412 (2002)

[24] P. K. Tien and J. P. Gordon, Phys. Rev. 129, 647 (1963)

[25] M. Büttiker *et al.*, Physical Review B 31 (10): 6207-6215 (1985)

[26] Landauer, IBM J. Res. Dev. 1, 223 (1957)

[27] M. Büttiker, Physical Review B 46 (19): 12485 (1992)

[28] K. Sabeeh *et al.*, Phys. Rev. B 78: 165420 (2008)

[29] T. Martin and R. Landauer, Phys. Rev. B 45 (4): 1742-1755 (1992)

[30] U. Fano, Phys. Rev. 124: 1866-1878 (1961)

[31] C. Chin *et al.*, Rev. Mod. Phys. 82, 1225-1286 (2010)

[32] R.C. Alig *et al.*, Phys. Rev. B 22, 5565-5582 (1980)

[33] C. W. J. Beenakker *et al.*, Phys. Rev. Lett. 96, 246802 (2006)

[34] R. Danneau *et al.*, Phys. Rev. Lett. 100, 196802 (2008)

[35] W. Li and L. E. Reichl, Phys. Rev. B 60, 15732-15741 (1999)

[36] F. Bagwell and R.K. Lake, Phys. Rev. B 46, 15329-15336 (1992)

Appendix A

Landauer conductance derivation

Here we derive a formula for conductance through a static graphene barrier. On the way, we introduce several important approximations including low potential across the sample and zero temperature. We start with the formula (3.16) derived in Chapter 3:

$$I_x = \frac{e\,v_f}{4\pi^2}\iint \mathrm{d}k\mathrm{d}\phi\, s\, e^{i\phi}\, T(k,\phi)\, f(E(k)) \tag{A.1}$$

Now all functions in the integrand are real apart from $e^{i\phi} = \cos\phi + i\sin\phi$. $T(k,\phi)$ and $f(E(k))$ are even in ϕ, thus the imaginary part of the integral is odd due to $\sin\phi$ and turns to zero under integration. We are left only with real part:

$$I_x = \frac{e\,v_f}{4\pi^2}\iint \mathrm{d}k\mathrm{d}\phi\, s\, T(k,\phi)\cos\phi\, f(E(k)) \tag{A.2}$$

At this point we should note that the integration over ϕ in (A.2) runs over the entire circle, while angles from $-\frac{\pi}{2}$ to $\frac{\pi}{2}$ correspond to the waves coming from the left, and the waves with ϕ from $\frac{\pi}{2}$ to $-\frac{\pi}{2}$ come from the right. Therefore, they will have different Fermi distributions, corresponding to L and R reservoirs.

$$\begin{aligned} I_x = \tfrac{e\,v_f}{4\pi^2}\int \mathrm{d}k \Bigg(&\int\limits_{-\pi/2}^{\pi/2} \mathrm{d}\phi\, s\, T(k,\phi)\cos\phi\, f_L(E(k)) + \\ + &\int\limits_{\pi/2}^{-\pi/2} \mathrm{d}\phi\, s\, T(k,\phi)\cos\phi\, f_R(E(k)) \Bigg) \end{aligned} \tag{A.3}$$

Now we can use the evenness property of the integrand again, and flip the second integral, arriving at the following expression:

$$I_x = \frac{e\,v_f}{4\pi^2}\int \mathrm{d}k \left(\int_{-\pi/2}^{\pi/2} \mathrm{d}\phi\, s\, T(k,\phi) \cos\phi \left(f_L(E(k)) - f_R(E(k)) \right) \right) \tag{A.4}$$

We encounter a difference between the Fermi functions to the right and to the left of the barrier. In order to simplify this expression we expand Fermi function in Taylor series:

$$f(E,\mu) \approx f(E_F,E_F) + (E - E_F)\frac{\partial f(E_F,E_F)}{\partial \mu} + (\mu - E_F)\frac{\partial f(E_F,E_F)}{\partial \mu} \tag{A.5}$$

Here we assume that the system is at thermal equilibrium, thus the temperature is constant, and doesn't enter the expansion as a variable. Then, the Fermi function depends only on the energy of particles and chemical potential of the bath. Note, that we are expanding around the Fermi surface and only to the first order in each variable. Both, chemical potential and energy are expanded around E_F. Assume now that we apply a small potential V_{LR} across the sample, we can say that the chemical potentials are modified as $\mu_L = E_F + \frac{eV_{LR}}{2}$, $\mu_R = E_F - \frac{eV_{LR}}{2}$. The first two terms in equation (A.5) are identical for both reservoirs. Therefore, the difference between two Fermi functions can be approximated as:

$$f(E,\mu_L) - f(E,\mu_R) \approx (\mu_L - E_F)\tfrac{\partial f(E_F,E_F)}{\partial \mu} - (\mu_R - E_F)\tfrac{\partial f(E_F,E_F)}{\partial \mu} \tag{A.6}$$

Plugging in the expressions for chemical potentials we arrive at:

$$f(\mu_L) - f(\mu_R) = eV_{LR}\frac{\partial f(E_F,E_F)}{\partial \mu} \tag{A.7}$$

Before proceeding with the calculation, we have to clarify that during the expansion we actually assumed that in absence of external potential V_{LR} the chemical potentials in both reservoirs are identical and equal to E_F. It is valid for the setup considered in this work. In addition, chemical and thermal equilibriums are readily accessable since they usually imply the lowest state of energy for the system. Thus, formulas derived here bear a generic character, given there is enough time for relaxation in the reservoirs.

Here we introduce another approximation which will lead to big simplification in calculations. We assume temperature of the system to be zero.

Effectively it tells us that Fermi distributions are sharp, becoming Heaviside step functions centered at Fermi energy. Physically, it means that we assume no thermal excitations in the system. In zero-temperature limit the Fermi distribution becomes a step function centered at the Fermi energy:

$$\lim_{\Theta\to 0} f(E) = 1 - H(E - E_F), \quad \frac{\partial H(E - E_F)}{\partial E} = \delta(E - E_F) \tag{A.8}$$

Now let us validate this assumption as well. We know, that the scale, on which transmission probability changes is governed by $\frac{\hbar v_F}{d}$. The energy for the thermal excitations are on the order of $k_B T$. So let us find the temperatures for which thermal excitations start to play a role: $T_0 = \frac{\hbar v_F}{d k_B}$. We can see that it strongly depends on the width of the barrier. Modern transistors also suffer from this kind of leakages due to thermal excitations. Having a 100 nm barrier gives us a temperature limit over a thousand Kelvin, which is more than enough for room-temperature electronics. But a barrier of just 10 nm results in a temperature limit of around 180 K, which is much lower than room temperature. So, thermal excitations can actually play an importand role in this case.

Nevertheless, in this thesis we do not consider high-temperature limit. Removing temperature dependence by setting it to zero results in (A.4) being simplified to:

$$I_x = \frac{e\, v_f}{4\pi^2} \int \mathrm{d}k \int\limits_{-\pi/2}^{\pi/2} \mathrm{d}\phi\, s\, T(k,\phi) \cos\phi\, eV_{LR} \delta(E - E_F) \tag{A.9}$$

Again, naturally, our zero-temperature approximation results in all charge carriers brought to the equilibrium Fermi level, and delta function is signalling us about that. By changing the integration parameter from k to E we get:

$$I_x = \frac{e\, v_f}{4\pi^2}\, e\, V_{LR} \frac{1}{\hbar v_f} \int\limits_{-\pi/2}^{\pi/2} \mathrm{d}\phi\, s\, T(E_F,\phi) \cos\phi \tag{A.10}$$

The conductance of the system can therefore be obtained as:

$$G_x = \frac{I_x}{V_{LR}} = \frac{e^2}{2\pi h} \int\limits_{-\pi/2}^{\pi/2} \mathrm{d}\phi\, s\, T(E_F,\phi) \cos\phi \tag{A.11}$$

Appendix B

Noise in graphene. Time domain derivation

Here we perform a procedure similar to that in Chapter 3, but derive a general formula for noise in graphene with static potential barrier. We have to deal with four-operator product averages, but from Section 4.1.1 we already know, that we can split them into biproducts of two-operator averages, and the way we treat them was already described in Chapter 3. Using (3.12): $\left\langle \hat{a}_\alpha(t_1) a^\dagger_\alpha(t_2) \right\rangle = \left\langle 1 - \hat{a}^\dagger_\alpha a_\alpha \right\rangle e^{iE(t_2-t_1)/\hbar} = (1-f_\alpha)(E) e^{iE(t_2-t_1)/\hbar}$. Therefore, (4.2) is transformed into:

$$\begin{aligned} &\left\langle \hat{I}(t_1)\hat{I}(t_2) \right\rangle = \sum_{\alpha,\alpha''} \tfrac{e^2 v_f^2}{(2\pi)^4} \int \Big[\mathrm{d}k \mathrm{d}\phi \mathrm{d}k' \mathrm{d}\phi' \mathrm{d}k'' \mathrm{d}\phi'' \mathrm{d}k''' \mathrm{d}\phi''' \times \\ &\times \Big(f_\alpha(E) f_{\alpha''}(E'') \Delta_{\alpha\alpha'} \Delta_{\alpha''\alpha'''} \Psi^\dagger_\alpha \sigma_x \Psi'_{\alpha'} \Psi''^\dagger_{\alpha''} \sigma_x \Psi'''_{\alpha'''} + \\ &+ f_\alpha(E)(1 - f_{\alpha''}(E'')) \Delta_{\alpha\alpha'''} \Delta_{\alpha'\alpha''} \times \\ &\times e^{iE(t_1-t_2)/\hbar} e^{iE''(t_2-t_1)/\hbar} \Psi^\dagger_\alpha \sigma_x \Psi'_{\alpha'} \Psi''^\dagger_{\alpha''} \sigma_x \Psi'''_{\alpha'''} \Big) \Big] \end{aligned} \tag{B.1}$$

Here $\Delta_{\alpha\beta} = \delta_{\alpha\beta}\delta(k_\alpha - k_\beta)\delta(\phi_\alpha - \phi_\beta)\delta_{s_\alpha s_\beta}$. Now we already know how these delta functions work, and therefore will proceed ommitting those standing for valley and spin degeneracy, and will include them in the final formula only.

At this point, it is useful to recall that in order to calculate the noise we have to take projections of current operators along y-direction:

$$\hat{I}_x = \lim_{L\to\infty} \frac{1}{L} \int_0^L \mathrm{d}y \hat{I} \tag{B.2}$$

Dependence on y coordinate comes in only with wavefunctions, and in the form of $e^{ik_y y}$. The product $\Psi^\dagger(E,x,y)\Psi(E',x,y)$ will project itself as:

$$\begin{aligned}&\lim_{L\to\infty}\frac{1}{L}\int_0^L \mathrm{d}y\Psi^\dagger(E,x,y)\Psi(E',x,y)=\lim_{L\to\infty}\frac{1}{L}\int_0^L \mathrm{d}y\Psi^\dagger(E,x)\Psi(E',x)e^{i(k'_y-k_y)y}=\\&=\Psi^\dagger(E,x)\Psi(E',x)\lim_{L\to\infty}\frac{1}{L}\int_0^L \mathrm{d}y e^{i(k'_y-k_y)y}=\Psi^\dagger(E,x)\Psi(E',x)\delta(k'_y-k_y)\end{aligned} \tag{B.3}$$

Thus, in our integrand from four wavefunctions we get a product of two delta functions: $\delta(k_y-k'_y)\delta(k''_y-k'''_y)$. Now we can see that these and the delta functions resulting from reducing four- to two-operator product averages simplify our integration greatly. The noise is found to be:

$$\begin{aligned}&S_x(t_2-t_1)=\frac{e^2v_f^2}{(2\pi)^4}\sum_{\alpha,\alpha''}\int \mathrm{d}k\mathrm{d}\phi\mathrm{d}k''\mathrm{d}\phi''\Big[f_\alpha(E)f_{\alpha''}(E'')\Psi^\dagger_\alpha\sigma_x\Psi_\alpha\Psi''^\dagger_{\alpha''}\sigma_x\Psi''_{\alpha''}\Big]+\\&+e^2v_f^2\sum_{\alpha\neq\alpha''}\int \mathrm{d}k\mathrm{d}\phi\mathrm{d}k''\mathrm{d}\phi''\Big[f_\alpha(E)e^{iE(t_1-t_2)/\hbar}(1-f_{\alpha''}(E''))e^{iE''(t_2-t_1)/\hbar}\times\\&\times\Psi^\dagger_\alpha\sigma_x\Psi''_{\alpha''}\Psi''^\dagger_{\alpha''}\sigma_x\Psi_\alpha\delta_{k_yk''_y}\Big]-\langle\hat{I}_x(t_1)\rangle\langle\hat{I}_x(t_2)\rangle\end{aligned} \tag{B.4}$$

Now note that the product in the first integral can be split into two mutually independent integrals, thus cancelling with the last term. Putting $t_2-t_1=\tau$:

$$\begin{aligned}&S_x(\tau)=\frac{e^2v_f^2}{(2\pi)^4}\sum_{\alpha,\alpha''}\int \mathrm{d}k\mathrm{d}\phi\mathrm{d}k''\mathrm{d}\phi''\Big[f_\alpha(\hbar v_f k)\left(1-f_{\alpha''}(\hbar v_f k'')\right)\times\\&\times e^{iv_f(k-k'')\tau}\Psi^\dagger_\alpha(k,\phi)\sigma_x\Psi_{\alpha''}(k'',\phi'')\Psi^\dagger_{\alpha''}(k'',\phi'')\sigma_x\Psi_\alpha(k,\phi)\delta_{k_yk''_y}\Big]\end{aligned} \tag{B.5}$$

Here we clearly can see that $\Psi^\dagger_\alpha(k,\phi)\sigma_x\Psi_{\alpha''}(k'',\phi'')\Psi^\dagger_{\alpha''}(k'',\phi'')\sigma_x\Psi_\alpha(k,\phi)=|\Psi^\dagger_\alpha(k,\phi)\sigma_x\Psi_{\alpha''}(k'',\phi'')|^2$. Thus, the equation for noise reduces to:

$$\begin{aligned}&S_x(\tau)=\frac{e^2v_f^2}{(2\pi)^4}\sum_{\alpha,\alpha''}\int \mathrm{d}k\mathrm{d}\phi\mathrm{d}k''\mathrm{d}\phi''\Big[f_\alpha(\hbar v_f k)\left(1-f_{\alpha''}(\hbar v_f k'')\right)\times\\&\times e^{iv_f(k-k'')\tau}|\Psi^\dagger_\alpha(k,\phi)\sigma_x\Psi_{\alpha''}(k'',\phi'')|^2\delta_{k_yk''_y}\Big]\end{aligned} \tag{B.6}$$